https://doi.org/10.1016/j.buildenv.2023.110844

Experimental and numerical study of an energy-efficient building fenestration system with seasonal adaptability

Chuyao Wang [1 *], Hongxing Yang [1 *], Jie Ji [2].

[1]Renewable Energy Research Group (RERG), Department of Building Environment and Energy Engineering, The Hong Kong Polytechnic University, Hong Kong, China

[2]Department of Thermal Science and Energy Engineering, University of Science and Technology of China, Hefei, China

Abstract

Previous building-integrated solar thermal fenestrations were limited to the single function, either air heating or water heating. Thus, they failed to meet the seasonal thermal needs of buildings. To address this limitation, this paper proposed a novel building fenestration-integrated solar collector. This system is designed to harness solar irradiation on the fenestrations for air heating in winter and recover irradiation for water heating in summer, effectively addressing seasonal thermal demands and improving annual solar utilization efficiency. Firstly, the prototype of the proposed system was fabricated, and its thermal performance was tested. The experimental results indicated the thermal efficiency of 40~50% for air heating and 39% for water heating. Subsequently, a mathematical model of the proposed system was developed and experimentally validated. Based on the validated model, a comparative performance analysis was conducted between the proposed system and double clear glazing. Additionally, the energy-saving potential and economic viability of the proposed system were predicted. Compared to double clear glazing, the proposed system exhibited a higher solar heat gain coefficient (SHGC) in air heating mode, lower SHGC in water heating mode, and lower U value at night. The prediction outcomes underscored the substantial energy-saving advantages conferred by the proposed system across diverse building types. The projected payback periods in subtropical and tropical regions were estimated to be around 2~4 years.

Keywords: Building energy saving; Fenestration system; Solar collection; Experiment test; Simulation analysis.

Nomenclature

Abbreviation

BIST Building integrated solar thermal

FISC Fenestration integrated solar collector

DGF Double glazed façade

DCG Double clear glazing

SHGC Solar heat gain coefficient

ROI Return on investment

Symbol

A area (m^2)

C heat capacity (J/kgK)

D thickness (m)

h heat transfer coefficient (W/m^2K)

R Thermal resistance (m^2K/W)

H height of the cavity (m)

I absorbed solar radiation (W/m^2)

L depth (m)

Nu Nusselt number

Pr Prandtl number

Ra Rayleigh number

ϕ latitude angle (rad)

σ azimuth angle (rad)

sw blind width (m)

R reflectance rate

si blind tilt angle (rad)

hs projected sun altitude angle (rad)

θ critical angle (rad)

F view factor

J radiant intensity (W/m^2)

G incident solar radiation (W/m^2)

τ transmittance

γ reflectance

α absorbance

T temperature (K)

v airflow rate (m/s)

ρ density (kg/m^3)

σ Stefan-Boltzman's constant (W/m^2K^4)

ς emissivity

λ thermal conductivity (W/mK)

Br temperature coefficient (K^{-1})

Subscript

a cavity air

c convection heat transfer

r radiative heat transfer

g,o outer glazing

g,i inner glazing

b solar blind

p copper pipe

w water

amb ambient air

e outdoor effective radiation temperature

$room$ indoor air

1

1. Introduction

According to the report by International Energy Agency, the building operations account for 30% of global final energy consumption, with almost half of it comes from air and water heating [1]. Solar collection, a technology with roots dating back to ancient times, can directly convert solar radiation into heat [2]. Building Integrated Solar Thermal (BIST) technology, which combines solar collectors with the building envelope, has garnered increasing attention due to its clean and pollution-free nature, cost-effectiveness, and ease of implementation [3]. The BIST technology is commonly employed in walls and roofs. However, in modern commercial buildings, the fenestration components, such as curtain walls, windows, and skylights, not only occupy a significant area but also represent the weakest part of the building's insulation structure [4]. By integrating BIST technology into the fenestration components, the utilization of solar energy in buildings can be enhanced, while simultaneously improving the thermal insulation performance of these components [5]. To date, extensive research has been conducted on the BIST fenestration components.

The air flow double glazed façade (DGF) is a prevalent fenestration system used for solar collection, comprising two glass layers with an air gap in between [6]. The air flow within the gap is utilized to recover heat from the glass for air preheating, which can be classified into return air and supply air based on the airflow direction. Concerning the return air, indoor air is employed to extract heat from the glass. Erell et al. [7] introduced a ventilated reversible glazing system capable of capturing heat on the absorptive glazing for space heating in winter and exhausting it in summer. The subsequent experimental and theoretical investigations demonstrated that this modified system substantially enhanced indoor human comfort [8]. Chow et al. [9] investigated the energy consumption performance of this ventilated reversible glazing system in subtropical and temperate climate zones. It was found that the reversible features were primarily required in subtropical regions. Wang et al. [10] and Guo et al. [11] proposed a double-skin ventilation window that utilized indoor return air to capture heat on the photovoltaic glass during winter. The energy performance in different climate regions was predicted. Concerning the supply air, outdoor air is preheated through the air gap and subsequently supplied into the room. Baker et al. [12] conducted experimental research on the

influence of weather parameter on the solar collector performance of a supply air window. Carlos et al. [13] analyzed the performance of heat recovery and solar collection of the ventilated double window in the supply air mode, followed by optimizing the system's structure to achieve a higher temperature rise of the supply air [14]. Michaux et al. [15] investigated the thermal performance of a supply air window and compared it with a conventional double skin window. The results revealed that the supply air window not only reduced the building's thermal demand but also improved the insulation performance. Huang et al. [16] explored the thermal insulation performance of the supply air double window by the hot box method, noting that the air flow rate of the supply air had a significant impact on the thermal insulation performance.

The water flow DGF is another innovative fenestration structure that harnesses heat on the glass by filling the middle channel of the double glazing with water [17]. Due to water's superior heat transfer properties compared to air, the water flow DGF generally exhibits higher solar collector efficiency than the air flow DGF. Chow et al. [18] firstly proposed the water flow window as water-preheating device. The simulation analysis indicated that indoor heat gain was reduced by 32% compared to the double skin window. Furthermore, the economic analysis demonstrated a payback period of less than 5 years for the system in Hong Kong [19]. Lyu et al. [20] studied the impact of design configurations on the thermal performance of the water flow window, finding that a water flow thickness of 15-20 mm and a height-to-width ratio of 0.4 were optimal parameters. The subsequent studies by various authors focused on further enhancing energy performance and practicality through new construction optimizations, including the use of anti-freeze liquid [21], vacuum glazing [22], geothermic [23], and phase change materials [22]. Gutai et al. [24] conducted a global analysis of the thermal performance of water flow DGF to evaluate its viability. The results indicated the potential energy savings ranged from 9% to 84% depending on the climate scenario. Wang et al. [25] proposed a smart water flow DGF by the integration of the electrochromic glass and the water flow, which not only collected heat on the glass but also enabled dynamic daylight modulation. The investigation results showed that this system could achieve a higher solar efficiency, reaching up to 42% compared to the conventional water flow DGF systems.

The clear fenestration systems allow a significant amount of solar irradiation to enter the room,

which can lead to the issues such as glare, thermal discomfort, or potential furniture damage. To address these issues, many commercial building fenestration systems are equipped with additional shading devices [26]. However, these shading devices usually absorb solar radiation, leading to an increase in temperature, and thus, act as a heat source for the fenestration. As a result, researchers explored the use of air or water to collect heat from these shading devices, leveraging their opaque characteristics to achieve higher thermal efficiency. Regarding air heating, Onur. et al [27] proposed an air window collector featuring vertical black blinds, and the thermal efficiency of this system was tested. Jalil et al. [28] investigated a window solar collector equipped with absorber blinds, assessing the air heating performance under various slat angles, mass flow rates, and irradiation intensities. Chialastri et al. [29] constructed a solar air collector for building fenestration applications, incorporating PV shading within the middle gap of the DGF. Zhang et al. [30] proposed a ventilation window with blinds, which reduced heat loss through the window by utilizing exhaust air. Regarding water heating, Ulavi et al. [31] introduced a hybrid solar window that incorporated a water pipe located at the focal point of a compound parabolic collector to collect heat. The investigation results indicated that the proposed system achieved comparable solar heat gain coefficients and thermal insulation performance to existing glazing technology while offsetting the water heating load. Shen et al. [32] embedded the cooling pipes in the venetian blinds of DGF to capture heat from the blinds. The simulation results demonstrated that the approximately 60% of the solar irradiation could be extracted by the cooling water. The authors further explored the cooling effects achieved by using groundwater [33] and evaporative cooling water [34] to decrease the temperature of the blinds.

Based on the literature reviews above, it can be concluded that the solar collection through fenestration systems is gaining popularity as a building integrated solar thermal (BIST) technology. However, the current development of fenestration systems only focuses on either air heating or water heating functions, which fails to meet the seasonal thermal demands of buildings and is therefore unsuitable for regions with cold winters and hot summers. With air heating systems, the introduction of warm air increases the building's cooling load and can even lead to indoor overheating in summer. While some studies have explored altering the airflow path to remove heat from the glass or shading [10, 35], the cooling effect remains limited due to the poor heat exchange capability of air.

Furthermore, the heat from the fenestration system is released into the environment along with the ventilation air, resulting in low utilization efficiency of solar energy. As for water heating systems, reducing indoor heat gain often results in increased building heating load in winter. Moreover, in high latitude areas, these systems are prone to freezing in waterways, rendering them inoperable without costly anti-freeze measures.

To address the aforementioned challenges, this paper proposes a novel building fenestration-integrated solar collector (FISC) system. This system incorporates a solar blind positioned within the cavity of a double-skin ventilation window, with a water pipe welded behind the blind for water circulation. In winter, the blind is cooled by indoor return air. The thermal performance of fenestrations is improved, because the blinds have a high solar absorbance rate. In summer, the solar blind is cooled by water, resulting in a significant reduction in indoor heat gain. Furthermore, the heat on the blind is recovered to produce hot water. To the best of the authors' knowledge, no similar structures have been reported in previous literature. This system integrates air heating and water heating functions into a single system, enabling the collection of solar radiation on building fenestration to generate warm air in winter and hot water during other seasons. Consequently, compared to conventional fenestration systems, the FISC system improves the annual thermal efficiency of solar collection and meets the building's seasonal thermal needs.

2. System description and experimental setup

2.1. Structure and working principle

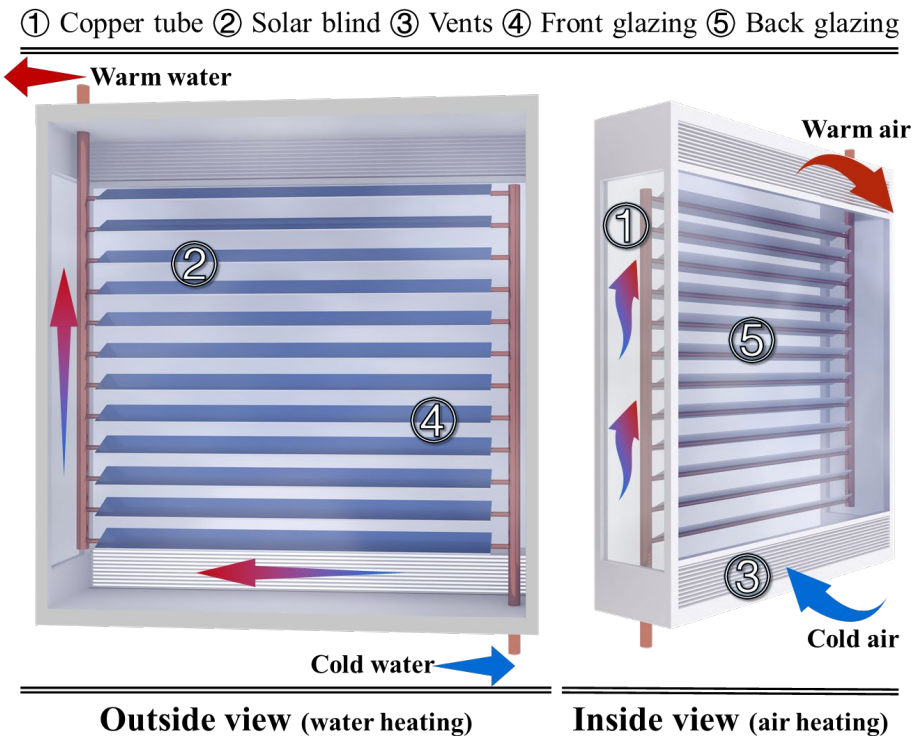

Fig. 1 The structure and working principle of the FISC system

Fig. 1 illustrates the appearance of the FISC system from both inside and outside views. The system comprises three layers: front glazing, back glazing, and a middle solar blind. Two vents are located at the bottom and top of the back glazing to connect the cavity air with indoor air. The solar blind serves as the core component of the system, consisting of an absorber slat and a copper water pipe. The copper water pipe is welded on the backside of the absorber slat, while the front side is coated with a selective absorption coating. The inlet and outlet header pipes are connected to the left and right ends of all copper pipes, respectively. The working principle of the proposed system, depicted in Fig. 1, involves two modes: air heating mode and water heating mode. During the heating season, the air heating mode is adopted. The water in the copper pipe is drained and the vents are opened. Solar irradiation absorbed by the solar blind is converted into heat. Driven by the fans, the cold air from the room enters the cavity, passes through the blinds, and is heated before being released back into the room, resulting in a reduction of the building heating load. In the non-heating seasons, the

water heating mode is utilized. The vents are closed, and the fans are turned off. Driven by the water pump, the cold water enters through the inlet of the copper pipe, absorbs heat from the solar blind, and exits through the outlet. This cooling effect on the blinds reduces indoor heat gain, thereby reducing the building cooling load in summer. Additionally, it provides a source of domestic hot water. The aforementioned working principle demonstrates that the FISC system achieves the comprehensive utilization of solar irradiation in different seasons. Compared to conventional fenestration, the FISC system meets the seasonal building thermal demand while offering a higher annual utilization efficiency of solar energy. Furthermore, in addition to the aforementioned operation modes, the fans and water pump of the proposed system are turned off at night. The solar blinds reduce convective heat transfer within the air cavity on one hand, and block a portion of the radiative heat transfer between the front and back glazing on the other hand. As a result, the thermal insulation performance of the fenestrations is enhanced.

2.2. Actual fabrication

The fabrication process and actual picture of the FISC system are shown in Fig. 2. Firstly, the solar absorber panels were cut into 1 m long and 8 cm wide fins, and then copper tubes were welded to the backside of the fins using laser welding. Secondly, a total of 12 fins with copper pipes were fixed to the header tube in parallel using laser welding, forming the solar blind group. The fins were inclined at the angle of 50°, and there was the 8cm space between the fins. The inlet and outlet of the header tube were threaded to facilitate connection to the water circuit. Finally, the solar blind group was installed in the middle of the frame, and two pieces of tempered glass were installed as the inner and outer layers. The overall dimensions of the system are 1.2 m wide, 1.3 m high, and the thickness of the air cavity is 0.15m. The frame was covered with 5 cm of insulation on the inside to reduce heat loss. Three axial fans were placed at the top of the inner glass, which was cut with three holes, and the bottom of the inner glass was cut with an opening measuring 0.15 m high and 1.2 m long for ventilation. At this stage, the FISC system was fully fabricated in preparation for the subsequent experimental phase. The geometric and physical information of the fabricated FISC system is listed

in Table 1. For the produced FISC system, the selective coating employed on the front side of the blind is the blue titanium film. Notably, this coating exhibits high absorbance in the solar spectrum and is commonly used in manufacture of solar collectors. The solar absorber panels used in the fabricated FISC systems were procured from a local company, Fujian Xinyue Metal Material Technology Co. According to the manufacturer's product manuals, the average solar absorbance of the selective coating was approximately 0.95.

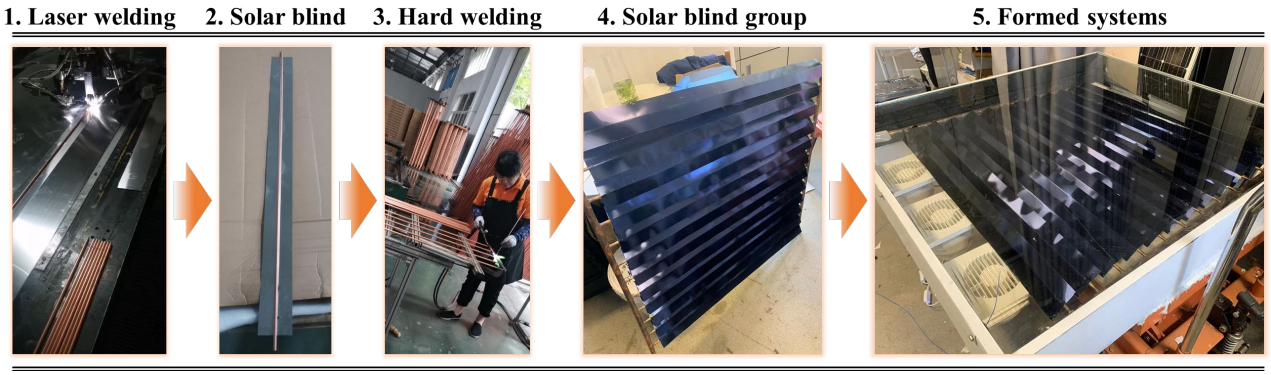

Fig. 2 The fabrication process and actual picture of the FISC system

Table 1 The geometric and physical information of the fabricated FISC system

Parameters		Value
Outer glazing	Thickness	0.005 m
	Specific heat capacity	840 J/(kg·K)
	Density	2500 kg/m^3
	Transmittance	0.79
	Reflectance	0.073
Inner glazing	Thickness	0.005 m
	Specific heat capacity	840 J/(kg·K)
	Density	2500 kg/m^3
	Transmittance	0.79
	Reflectance	0.073
Solar blind group	Specific heat capacity	880 J/(kg·K)
	Density	2750 kg/m^3
	Slat width	0.08 m
	Slat thickness	0.001 m
	Slat space	0.08 m
	Slat angle	50°
	Solar absorbance (front)	0.95

	Solar absorbance (back)	0.15
	Number	12
	Inner diameter	0.007 m
	Thickness	0.001 m
Copper pipe	Specific heat capacity	385 J/(kg·K)
	Density	8933 kg/m^3
	Heat conductivity	397 W·m^{-2}·K^{-1}

2.3. Experimental setup

The thermal performance of the FISC system was tested in the indoor laboratory. The test apparatus included thermocouples, platinum resistor, pyranometer, flow meter, and anemograph. The specification and parameters of these apparatus are listed in the Table 2. The layout of experimental equipment and test apparatus is shown in Fig. 3. A solar simulator (HONLE SOL 2000 matrix) was employed to deliver solar radiation to the system. The solar simulator consists of eight independent xenon lamps and can cover a test area measuring 2.5 m×2.5 m. Each lamp measures 397 mm in length and 305 mm in width, with a rated power of 2000 W. The simulator's alignment with the AM1.5 solar spectrum, spatial uniformity, and temporal stability align with the criteria stipulated by the IEC 60904-9 standard for solar simulators. The distance separating the solar simulator from the test bed was 2 meters. An 80 L water tank was utilized to store the hot water generated by the system, with the water flow between the tank and the collector facilitated by a water pump. A pyranometer was employed to measure the irradiation incident on the FISC system. The cavity air velocity of the system was measured using an anemograph placed in the middle of the air cavity. A platinum resistor was employed to measure the water temperature in tank. A flow meter was used to measure the water flow rate in the circulation. The position of temperature measuring point in FISC system is shown in Fig. 4. To obtain a representative measurement of the average temperature of the inlet and outlet air, two platinum resistances are strategically placed in the middle of the top and bottom vents, respectively. Before conducting the experiment, the temperature testing across various positions along the width of vents was conducted. The test results revealed that the temperature variations in the width direction is within the range of the measurement error of used temperature sensor. Therefore, the air

temperature measurements at the middle points of the vents are indicative of the average temperature of the inlet and outlet air. Three thermocouples were placed at the middle position of the back sides of the second, sixth, and tenth blinds in the FISC system to measure the upper, middle, and lower temperatures of the solar blind group. Another thermocouple was used to measure the temperature of outer glass. To against external radiation effects, all temperature sensors were encased in anti-radiation film. All sensors were connected to a data logger, and data acquisition frequency was once per second during the experimental period.

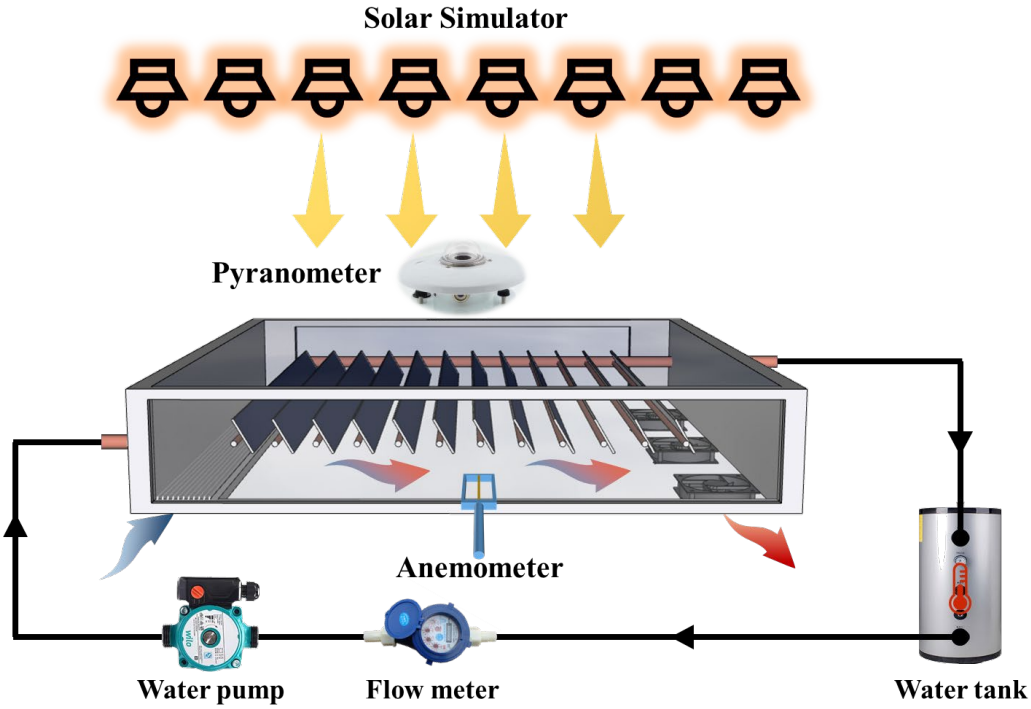

Fig. 3 The layout of experimental equipment and test apparatus

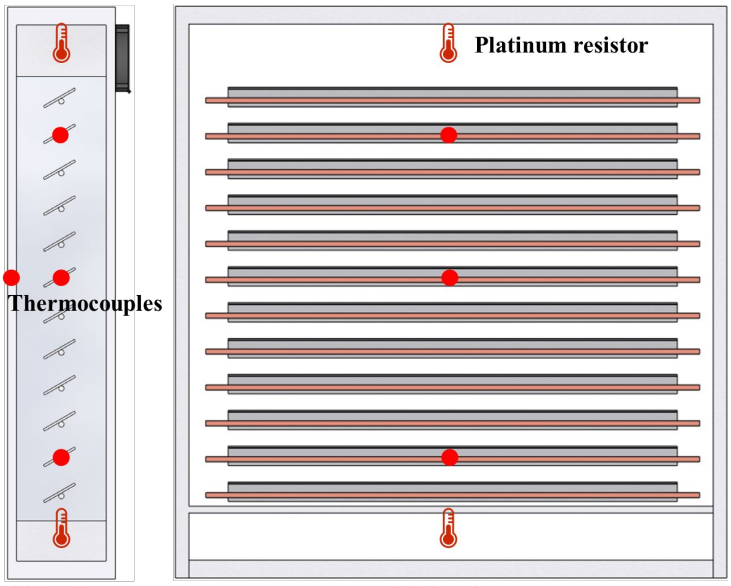

Fig. 4 The position of temperature measuring point in FISC system

Table 2 The list of experimental sensors and monitoring devices

Experimental equipment		Specification	Uncertainty
Thermocouple		Type T	±0.5℃
Platinum resistor		Pt 100	±0.2℃
Pyranometer		EKO MS-802	±0.2%
Flow meter		LXS-15CE	±1%
Anemograph		VELOCICALC®Plus 8386	±0.015m/s
Data logger		MIDI LOGGER GL840	/

The actual appearance of the experimental setup is shown in Fig. 5. This study examined three distinct levels of irradiation, which are respectively 475 W/m² for four lamps, 540 W/m² for six lamps, and 780 W/m² for eight lamps. During the experimental period, the thermal performance of the FISC

system was tested separately in air heating and water heating modes. In the air heating mode, the vents were opened, and the fans were turned on, while the water pump remained off. The indoor temperature was controlled at 25.5℃ by the air conditioner. The FISC system operated under a constant irradiation until a steady temperature field was established. The air velocity in the cavity was regulated by adjusting the power of fans. The experiments under the air velocities of 0.3 and 0.6 m/s were conducted in this study. By combining different air velocities and different levels of irradiation, a total of 6 sets of experimental data were obtained for the air heating mode. In the water heating mode, a closed loop was established between the water tank and the collector, driven by the water pump with a constant flow rate. The flow meter recorded a water flow rate of approximately 15 L/min. The system operated under each level of irradiation for a duration of 5 hours, with the initial water temperature in the tank measured to be around 26℃. All experimental cases and the corresponding test conditions are listed in Table 3.

Table 3 The input parameters of experimental cases

		Solar irradiation (W/m^2)	Air velocity (m/s)	Water flow rate (L/min)
Air heating	Case 1	475	0.3	/
	Case 2	540	0.3	/
	Case 3	780	0.3	/
	Case 4	475	0.6	/
	Case 5	540	0.6	/
	Case 6	780	0.6	/
Water heating	Case 1	475	/	15
	Case 2	540	/	15
	Case 3	780	/	15

(a) Solar simulator (b) Test rig

Fig. 5 The actual appearance of the experimental setup

3. Mathematical model

The energy flow within the FISC system involves conduction, convention, long-wave and short-wave radiation. Additionally, there are enthalpy flows of air and water within the vertical cavity and horizontal pipe, respectively. To simulate this system, the absorption of solar radiation by the glasses and blind is first determined and then incorporated into the heat transfer models. In this section, the optical and heat transfer models of the FISC system were respectively introduced. To strike a balance between model accuracy and complexity, several general assumptions were made: (a) the temperature of air and water changed only along the flow direction; (b) the irradiation reflected by the blinds was considered purely diffuse; and (c) the temperature of the glass and blind was assumed to be uniform in the thickness direction due to their small thickness.

3.1. Solar absorbance and transmittance

The optical behaviors of the double-skin window with blind have been extensively developed and validated in our earlier research [36]. In this section, the model for calculating solar absorbance and transmittance of the system is briefly introduced. The detailed references can be found in our previous works. Both the inner and outer glasses are typical transparent mediums. The solar transmittance, reflectance, and absorbance of glass have been thoroughly detailed and summarized in ISO 9050. The resulting calculation outcomes are presented as follows:

$$\tau_g = \frac{t(1-r)^2}{1-t^2r^2} \quad (1)$$

$$\gamma_g = r[1 + \frac{t^2(1-r)^2}{1-t^2r^2}] \quad (2)$$

$$\alpha_g = 1 - \tau - \gamma \quad (3)$$

where, t and r depend on the solar incident angle by Bouger's law and Fresnel's law.

The optical behavior of the solar blind constitutes the primary complexity in terms of the solar absorbance and transmittance of the FISC system. The interaction of the irradiation within the blind cavity depends on the projected solar altitude angle. As illustrated in Fig. 6, when the projected solar altitude angle exceeds the critical angle, all beam radiation is incident on the solar blind. Conversely, when the projected solar altitude angle is below the critical angle, a portion of the beam radiation passes through the blinds, and the front side of the blinds is entirely exposed to the beam radiation. In Fig. 6, *si* represents the slat angle of blind and *hs* represents the projected solar altitude angle. The projected solar altitude angle and critical angle are respectively calculated by [37]:

$$hs = arctan\left(\frac{sin\,(\phi)}{cos\,(\sigma_{sun}-\sigma_g)cos\,(\phi)}\right) \quad (4)$$

$$\theta = arctan\left(\frac{1-sin\,(si)}{cos\,(si)}\right) \quad (5)$$

where, ϕ is the solar altitude angle. σ_{sun} and σ_g respectively represent the azimuth of the sun and FISC system.

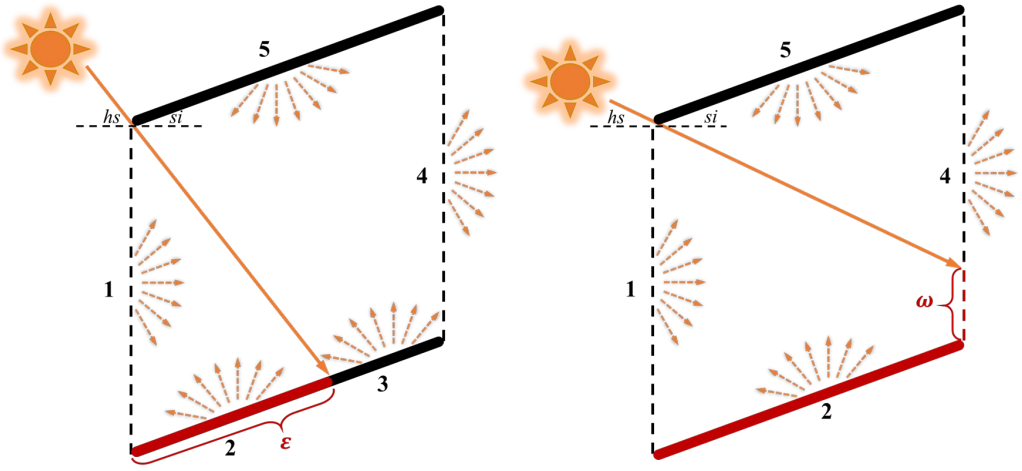

Fig. 6 Schematic of the interaction of the outside irradiation in the blind cavity

ε represents the fraction of the blind that is not shaded, while ω signifies the transmittance of beam irradiation that passes through the blind. These values are calculated using the following formulas:

$$\begin{cases} \varepsilon = 1 \\ \omega = 1 - \frac{(sin(si)+cos\,(si)tan\,(hs))}{1}, \ hs < \theta \end{cases} \tag{6}$$

$$\begin{cases} \varepsilon = \frac{1}{sin(si)+cos\,(si)tan\,(hs)}, \ hs \geq \theta \\ \omega = 0 \end{cases} \tag{7}$$

The solar transmittance of beam radiation for solar blind is calculated by Equ (6-7). The solar transmittance of diffuse radiation and the solar absorbance are calculated by the radiosity method. As depicted in Fig. 6, the surfaces of the blind cavity are divided into five parts. Surface 1 corresponds to the outside of the blind cavity, while surface 4 pertains to the inside of the blind cavity. Surfaces 2 and 3 respectively represent the unshaded and shaded portions of the blind's front side. Surface 5 is the back side of the blind cavity. The radiosity equation set for all these surfaces is expressed as:

$$\begin{cases} J_1 = G_{d,v} \\ J_2\varepsilon = (G_{b,t}\varepsilon + J_1F_{1-2} + J_4F_{4-2} + J_5F_{5-2})R_f \\ J_3(1-\varepsilon) = (J_1F_{1-3} + J_4F_{4-3} + J_5F_{5-3})R_f \\ J_4 = 0 \\ J_5 = (J_1F_{1-5} + J_2\varepsilon F_{2-5} + J_3(1-\varepsilon)F_{3-5} + J_4F_{4-5})R_b \end{cases} \tag{8}$$

where, J_i represents the total radiation emitting from the *i* surface. $G_{d,v}$ is the diffusive irradiation from the outside of blind cavity. $G_{b,t}$ is the beam irradiation incident on the solar blind. R_f and R_b represent the blind reflectance of the front and back sides. *F* denotes the view factor between two surfaces.

After solving the Equ (8), the irradiation emitting from each surface is obtained. Then, the solar absorbance of the blind is calculated as:

$$\alpha_b = \left(J_2\varepsilon + J_3(1-\varepsilon)\right)\left(\frac{1}{R_f} - 1\right) + J_5\left(\frac{1}{R_b} - 1\right) \tag{9}$$

The diffuse irradiation through the blind is calculated as:

$$\tau_b = J_1F_{1-4} + J_2\varepsilon F_{2-4} + J_3(1-\varepsilon)F_{3-4} + J_5F_{5-4} \tag{10}$$

The irradiation reflected from the blind is calculated as:

$$\gamma_b = J_4F_{4-1} + J_2\varepsilon F_{2-1} + J_3(1-\varepsilon)F_{3-1} + J_5F_{5-1} \tag{11}$$

Once the solar transmittance, reflectance, and absorbance of the three layers are determined, the solar absorbance of each layer and the overall transmittance of the system can be calculated by summing the infinite reflections, absorptions, and transmissions between outer glass, inner glass, and solar blind. This is done using the net radiation method as described in the reference [38].

3.2. Heat transfer

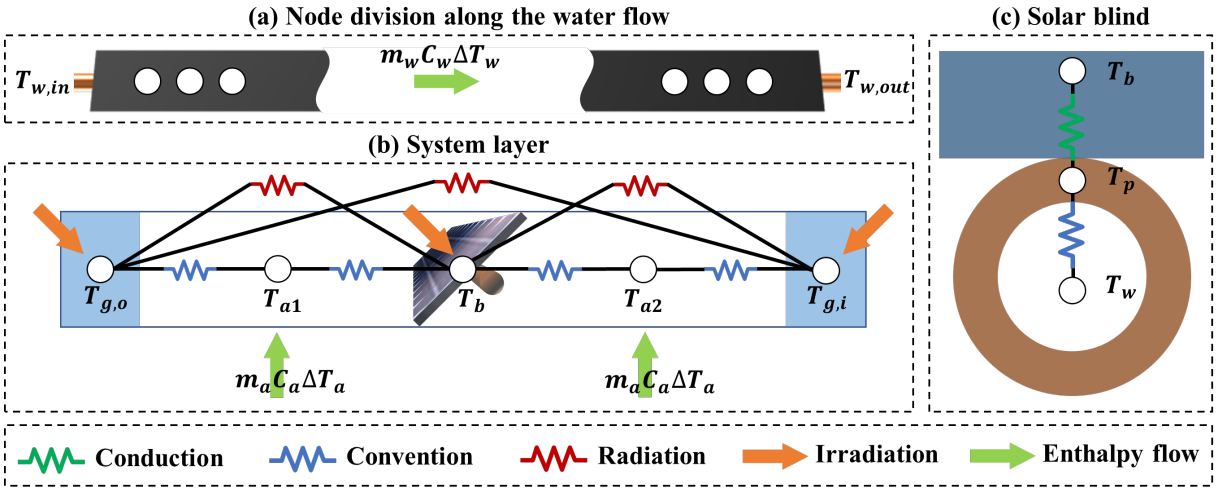

Fig. 7 The 3-D node distribution of heat transfer model of the FISC system

The 3-D node distribution of the heat transfer model is depicted in Fig. 7. The system consists of five layers in the depth direction: outer glass, outer air gap, solar blind, inner air, and inner glass. These layers are denoted by subscript 'g,o', '$a1$', 'b', '$a2$', and 'g,i'. The blind, water pipe, and water flow are discretized both horizontally and vertically, while the glass and air gap are only discretized vertically. The node numbers in the vertical and horizontal directions are represented by superscripts 'N' and 'M', respectively. The heat transfer model of the FISC system is obtained by applying the energy balance equation to the nodes.

The energy balance of outer glass includes the terms of conduction, long-wave radiation, and solar absorbance. The equation is written as:

$$(D\rho C)_{g,o}\frac{\partial T_{g,o}^{N}}{\partial t} = (D\lambda)_{g,o}\frac{T_{g,o}^{N+1}+T_{g,o}^{N-1}-2T_{g,o}^{N}}{\Delta z^{2}} + I_{g,o} + h_{r,go-e}\left(T_e - T_{g,o}^{N}\right) + h_{c,go-amb}\left(T_{amb} - T_{g,o}^{N}\right) + h_{r,go-b}\left(T_b - T_{g,o}^{N}\right) + h_{r,go-gi}\left(T_{g,i} - T_{g,o}^{N}\right) + h_{c,go-a1}\left(T_{a1} - T_{g,o}^{N}\right) \quad (12)$$

where, D and ρ represent the thickness and density while C and λ are the heat capacity and thermal conductivity. h_c and h_r are the convective and radiative heat transfer coefficients, respectively. I is the irradiation absorbed by the component. Δz is the distance between nodes in vertical direction. T_e and T_{amb} are outdoor effective radiation temperature and air temperature.

Similar with outer glass, the equation of inner glass is written as:

$$(D\rho C)_{g,i}\frac{\partial T_{g,i}^{N}}{\partial t} = (D\lambda)_{g,i}\frac{T_{g,i}^{N+1}+T_{g,i}^{N-1}-2T_{g,i}^{N}}{\Delta z^2} + I_{g,i} + (h_{c,gi-room} + h_{r,gi-room})\left(T_{room} - T_{g,i}^{N}\right) + h_{r,gi-b}\left(T_b - T_{g,i}^{N}\right) + h_{r,go-gi}\left(T_{g,o} - T_{g,i}^{N}\right) + h_{c,gi-a2}\left(T_{a2} - T_{g,i}^{N}\right) \quad (13)$$

The energy balance of air gap only includes the terms of convention and enthalpy flow. The equations are written as:

$$(D\rho C)_{a1}\frac{\partial T_{a1}^{N}}{\partial t} = h_{c,go-a1}\left(T_{g,o} - T_{a1}^{N}\right) + h_{c,b-a}(T_b - T_{a1}^{N}) - v_a(D\rho C)_{a1}\frac{T_{a1}^{N-1}-T_{a1}^{N}}{\Delta z} \quad (14)$$

$$(D\rho C)_{a2}\frac{\partial T_{a2}^{N}}{\partial t} = h_{c,gi-a2}\left(T_{g,i} - T_{a2}^{N}\right) + h_{c,b-a}(T_b - T_{a2}^{N}) - v_a(D\rho C)_{a2}\frac{T_{a2}^{N-1}-T_{a2}^{N}}{\Delta z} \quad (15)$$

where, v_a is the cavity air velocity.

The energy balance of solar blind includes the terms of conduction, convention, long-wave radiation, and solar absorbance. The equation is written as:

$$(D\rho C)_b\frac{\partial T_b^{N,M}}{\partial t} = I_b + h_{r,go-b}\left(T_{g,o} - T_b\right) + h_{c,b-a}(T_{a1} - T_b) + h_{c,b-a}(T_{a2} - T_b) + h_{r,gi-b}\left(T_{gi} - T_b\right) + h_{r,b-b}\left(T_b^{N+1,M} + T_b^{N-1,M} - 2T_b^{N,M}\right) + (D\lambda)_b\frac{T_b^{N,M+1}+T_b^{N,M-1}-2T_b^{N,M}}{\Delta y^2} + \frac{(T_p^{N,M}-T_b^{N,M})}{R} \quad (16)$$

where, Δy is the distance between nodes in horizontal direction. R is the equivalent thermal resistance between copper pipe and blind.

The energy balance of copper pipe depends on the work mode because the convention term only occurs when the water heating mode is used. In addition, the conduction heat transfer between the pipe and the aluminum slat, as well as the convection heat transfer between the pipe and the water, are significantly more pronounced compared to the natural convection heat transfer between the copper tube and the surrounding air [39]. As a result, the convection heat exchange between the pipe and air is neglected. The equation of copper pine is written as:

When the water heating function is used:

$$\pi d_w(\rho CD)_p \frac{\partial T_p^{N,M}}{\partial t} = \pi d_w(\lambda D)_p \frac{T_p^{N,M+1}+T_p^{N,M-1}-2T_p^{N,M}}{\Delta y^2} + \pi d_w h_{c,p-w}\left(T_w^{N,M} - T_p^{N,M}\right) + \frac{(T_b^{N,M}-T_p^{N,M})}{R} \quad (17)$$

When the water heating function is not used:

$$\pi d_w(\rho CD)_p \frac{\partial T_p^{N,M}}{\partial t} = \pi d_w(\lambda D)_p \frac{T_p^{N,M+1}+T_p^{N,M-1}-2T_p^{N,M}}{\Delta y^2} + \frac{(T_b^{N,M}-T_p^{N,M})}{R} \quad (18)$$

where, subscript 'p' and 'w' respectively represents the copper pipe and water in pipe. d_w is the inner diameter of water pipe.

The energy balance of water in pipe only occurs when the water heating mode is used and includes the terms of convention, conduction, and enthalpy flow. The equation is written as:

$$\frac{d_w}{4}(\rho C)_w \frac{\partial T_w^{N,M}}{\partial t} = \frac{d_w}{4}\lambda_w \frac{T_w^{N,M+1}+T_w^{N,M-1}-2T_w^{N,M}}{\Delta y^2} - \frac{d_w}{4}\rho_w v_w C_w \frac{T_w^{N,M-1}-T_w^{N,M}}{\Delta y} + h_{c,w-p}(T_p^{N,M} - T_w^{N,M}) \quad (19)$$

where, v_w is the water velocity.

The convective heat transfer coefficient between outer glass and outdoor air is related to the wind speed v_{amb}. The equation is written as [40]:

$$h_{c,go-amb} = 5.62 + 3.9v_{amb} \quad (20)$$

The convective heat transfer coefficient between inner glass and room air is written as [41]:

$$h_{c,room} = 2.03|T_{g,in} - T_{room}|^{1/3} \quad (21)$$

When the fan is on, the convective coefficients between glass and cavity air is calculated as: [40]:

$$h_{c,go/gi-a} = 5.62 + 3.9v_a \quad (22)$$

When the fan is off, the convective coefficients between glass and cavity air is calculated as [42]:

$$h_{c,go/gi-a} = \frac{Nu\cdot\lambda_a}{L_a} \quad (23)$$

$$Nu = (Nu_1, Nu_2)\max \quad (24)$$

$$Nu_1 = \begin{cases} 0.0673838Ra^{1/3}, Ra > 50000 \\ 0.028154Ra^{0.4134}, 500000 > Ra > 10000 \\ 1 + 1.7596678\times10^{-10}Ra^{2.2984755}, Ra < 10000 \end{cases} \quad (25)$$

$$Nu_2 = 0.242(\frac{Ra}{H/L_a})^{0.272} \quad (26)$$

where, Nu is the Nusselt number; Ra is the Rayleigh number; λ_a is the air thermal conductivity; H and L_a are the cavity height and depth, respectively.

When the fan is off, the convective coefficients on the blind surface is same as that between cavity and glass. When the fan is on, this convective coefficient is calculated as [43]:

$$h_{c,b-a} = \frac{Nu \cdot \lambda_a}{sw} \quad (27)$$

$$Nu = 0.51 Re^{0.5} Pr^{0.37} \quad (28)$$

where, sw is the width of the solar blind; Re is the Reynolds number of the cavity air flowing through blinds; Pr is the Prandtl number of cavity air.

In the proposed system, the length of the copper pipes far exceeds the diameter. This significant length-to-diameter ratio far exceeds the critical value for entrance region [44], indicating that the flow inside the tubes can be considered as fully developed. The convective coefficient between water and pipe wall in water pipe is calculated as [45, 46]:

$$h_{c,p-w} = \frac{Nu \cdot \lambda_w}{d_w} \quad (29)$$

$$Nu = \begin{cases} \frac{(f/8)(Re-1000)Pr}{1+12.7\sqrt{\frac{f}{8}}(Pr^{\frac{2}{3}}-1)}, \mathrm{Re} > 2300 \\ 3.66, \ \mathrm{Re} < 2300 \end{cases} \quad (30)$$

where, Re and Pr are the Reynolds number and Prandtl number of the water in pipe. f is the friction factor of pipe.

The radiative heat transfer coefficient between outer glass and outdoors is calculated as:

$$h_{r,\mathrm{go}-e} = \varsigma_g \sigma ({T_{g,o}}^2 + {T_e}^2)(T_{g,o} + T_e) \quad (31)$$

The radiative coefficients between inner glass and indoors is calculated as:

$$h_{r,gi-room} = \varsigma_g \sigma ({T_{g,i}}^2 + {T_{room}}^2)(T_{g,i} + T_{room}) \quad (32)$$

The radiative coefficient between inner glass and outer glass is calculated as:

$$h_{r,go-gi} = \frac{\sigma ({T_{g,o}}^2 + {T_{g,i}}^2)(T_{g,o} + T_{g,i})}{\frac{1}{\varsigma_{g,o}} + \frac{1}{\varsigma_{g,i}} - 1} \quad (33)$$

Both the front and back side of the blinds have radiation heat exchange with the outer glass. Thus, the radiative coefficient should be the sum of these two parts. The equation is written as:

$$h_{r,go-b} = \frac{\sigma({T_{g,o}}^2+{T_b}^2)(T_{g,o}+T_b)}{\frac{1}{\varsigma_{g,o}}+\frac{1}{\varsigma_{bf}}-2+\frac{1}{F_{g,o-bf}}} + \frac{\sigma({T_{g,o}}^2+{T_b}^2)(T_{g,o}+T_b)}{\frac{1}{\varsigma_{g,o}}+\frac{1}{\varsigma_{bb}}-2+\frac{1}{F_{g,o-bb}}} \quad (34)$$

Similarly, the radiative heat transfer coefficient between the blind and inner glass is written as:

$$h_{r,gi-b} = \frac{\sigma({T_{g,i}}^2+{T_b}^2)(T_{g,i}+T_b)}{\frac{1}{\varsigma_{bf}}+\frac{1}{\varsigma_{g,i}}-2+\frac{1}{F_{g,i-bf}}} + \frac{\sigma({T_{g,i}}^2+{T_b}^2)(T_{g,i}+T_b)}{\frac{1}{\varsigma_{bb}}+\frac{1}{\varsigma_{g,i}}-2+\frac{1}{F_{g,i-bb}}} \quad (35)$$

The radiative heat transfer coefficient between adjacent blinds is written as

$$h_{r,b-b} = \frac{\sigma({T_b}^2+{T_b}^2)(T_b+T_b)}{\frac{1}{\varsigma_{bb}}+\frac{1}{\varsigma_{bf}}-2+\frac{1}{F_{b-b}}} \quad (36)$$

where, ς_{go} and ς_{gi} are the emissivity of the outer and inner glass; ς_{bf} and ς_{bb} are the emissivity of the both sides of the blind; *F* is the view factor.

3.3. Solving method

The mathematical models of the FISC system were solved using the Matlab program. The flow chart of the solving process is shown in Fig. 8. The meteorological information and indoor temperature are inputted as the boundary conditions. To calculate the solar absorbance and transmittance of all components, the solar altitude angle, azimuth angle, and solar radiation are provided as inputs to the optical model. The resulting solar absorbance of all components is then utilized as inputs into the heat transfer models, respectively. The time derivative in the energy balance equation is discretized using a one-step forward difference. Subsequently, all heat transfer equations are solved through the iteration. Initially, assumed values, often temperatures from the previous time step, are assigned to all nodes. Following this, the heat transfer coefficients are calculated based on the temperatures of all nodes. Using these coefficients, the equations for outer glass, air gap, inner glass, blind, copper pipe, and water are sequentially solved. The calculated temperature results of all components are then used to derive new values for the heat transfer coefficients. Using the updated coefficients, the heat transfer equations for all components are solved again. This iterative process

continues until the temperature changes fall below a defined residual. After completing the iterative process, the program proceeds to the next time step.

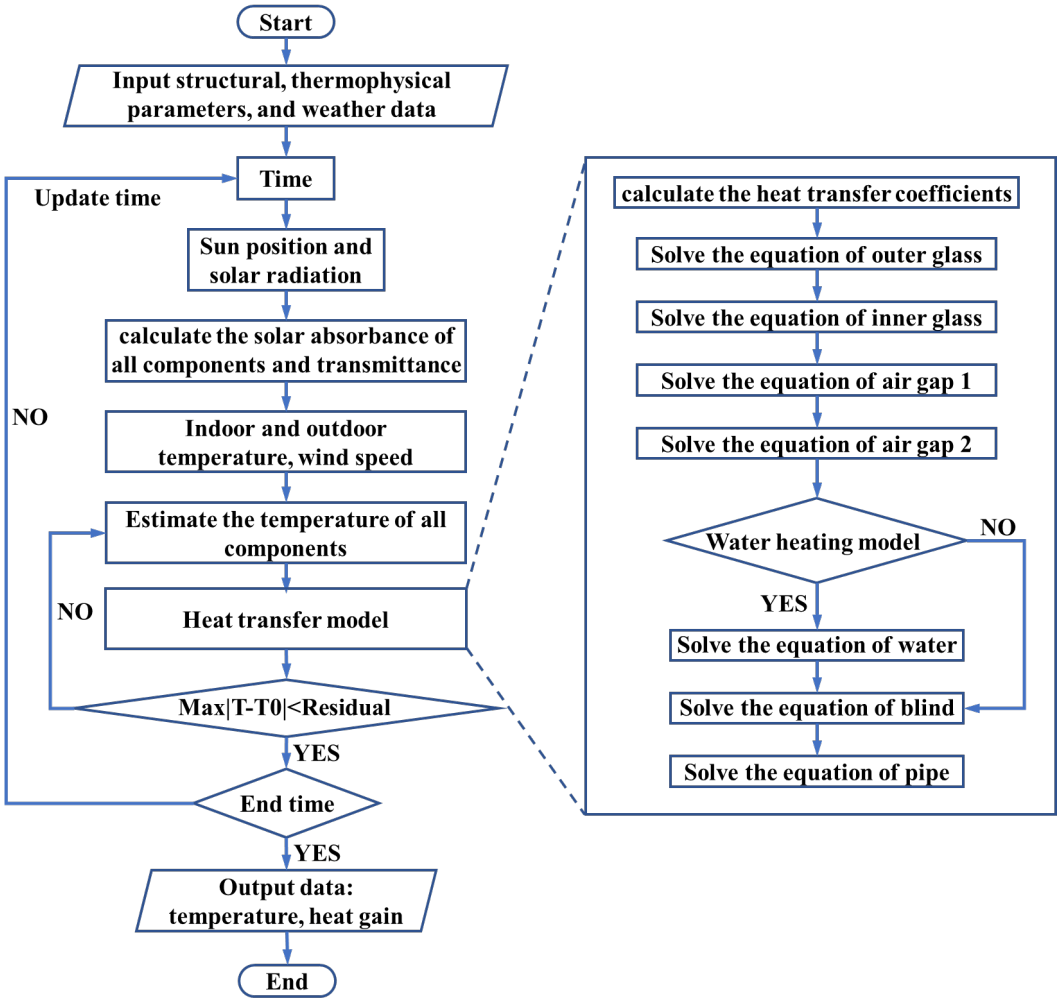

Fig. 8 The flow chart of solving process of mathematical mode

4. Results and discussion

4.1. Experimental results and model validation

In this section, the experimental results are thoroughly analyzed. Subsequently, the experimental data are employed to validate the mathematical model of the proposed system.

4.1.1. Evaluation indicators and uncertainty analysis

Before analyzing the experimental results, the thermal efficiency of the FISC system is defined.

When the FISC system works under the air heating mode, the thermal efficiency for heating air is calculated using the following formula [47]:

$$\eta_{th,a} = \frac{m_a C_a (T_{a,out} - T_{a,in})}{GA} \tag{37}$$

where, $\eta_{th,a}$ is the thermal efficiency for heating air. m_a and C_a are respectively mass flow rate and heat capacity of cavity air. $T_{a,out}$ and $T_{a,in}$ are respectively the temperatures of air outlet and air inlet. G represents the irradiation incident on the outer glazing and A is the area of the FISC system.

When the FISC system works under the water heating mode, the thermal efficiency for heating water is calculated using the following formula [47]:

$$\eta_{th,w} = \frac{\rho_w C_w V_w (T_{w,end} - T_{w,initial})}{GA\Delta t} \tag{38}$$

where, $\eta_{th,w}$ is the average thermal efficiency for heating water. ρ_w, C_w, and V_w are respectively density, heat capacity, volume of water in tank. $T_{w,end}$ and $T_{w,initial}$ are respectively the final and initial temperatures of tank water. Δt is the duration of the experiment.

The uncertainties of the measured data are listed in Table 2. The air and water thermal efficiencies are the parameters dependent on measured data. As a result, their uncertainties can be attributed to uncertainties of the measurement data. The uncertainties of thermal efficiencies are calculated using Equ (39) [48]. The results indicate that the average uncertainties of thermal efficiency are 6.8% for air heating and 1.9% for water heating. The uncertainties of thermal efficiency and measured data for each experimental case are represented by the error bars in the figure of the experimental results.

$$u_\eta = \sqrt{(\frac{\partial \eta}{\partial x_1})^2 u_1^2 + (\frac{\partial \eta}{\partial x_2})^2 u_2^2 + \cdots + (\frac{\partial \eta}{\partial x_n})^2 u_n^2} \tag{39}$$

where, u_η is the uncertainty of thermal efficiency. x_1 to x_n are the measured data in the calculation equation of thermal efficiency while u_1 to u_n are the corresponding measurement errors.

4.1.2. Experimental results

The experimental results of the FISC system under air heating mode are presented in Fig. 9. The solar blinds absorb the irradiation, leading to an increase in their temperature, which in turn transfers heat to the cavity air. As a result, the cavity air temperature remains lower than that of the solar blind.

The temperature rise of cavity air increases with the higher irradiation and decreases with the higher air velocity. This phenomenon occurs because at higher air velocity, the cavity air quickly flows out of the air cavity, leaving less time for heat exchange with the solar blind. When the air velocity is 0.3 m/s, the temperature rises of the cavity air are 8.1℃, 5.5℃, and 4.6℃ for eight, six, and four lamps turned on, respectively. The thermal efficiency for air heating ranges from 40% to 50% and varies with irradiation and air velocity. The thermal efficiency increases with higher solar radiation, as it leads to higher ambient temperatures around the system. Additionally, the thermal efficiency increases with higher air velocity. This is because higher air velocity enhances the heat transfer between the solar blind and the cavity air, and as mentioned earlier, the higher air velocity lowers the cavity air temperature, resulting in increased the heat gain of cavity air.

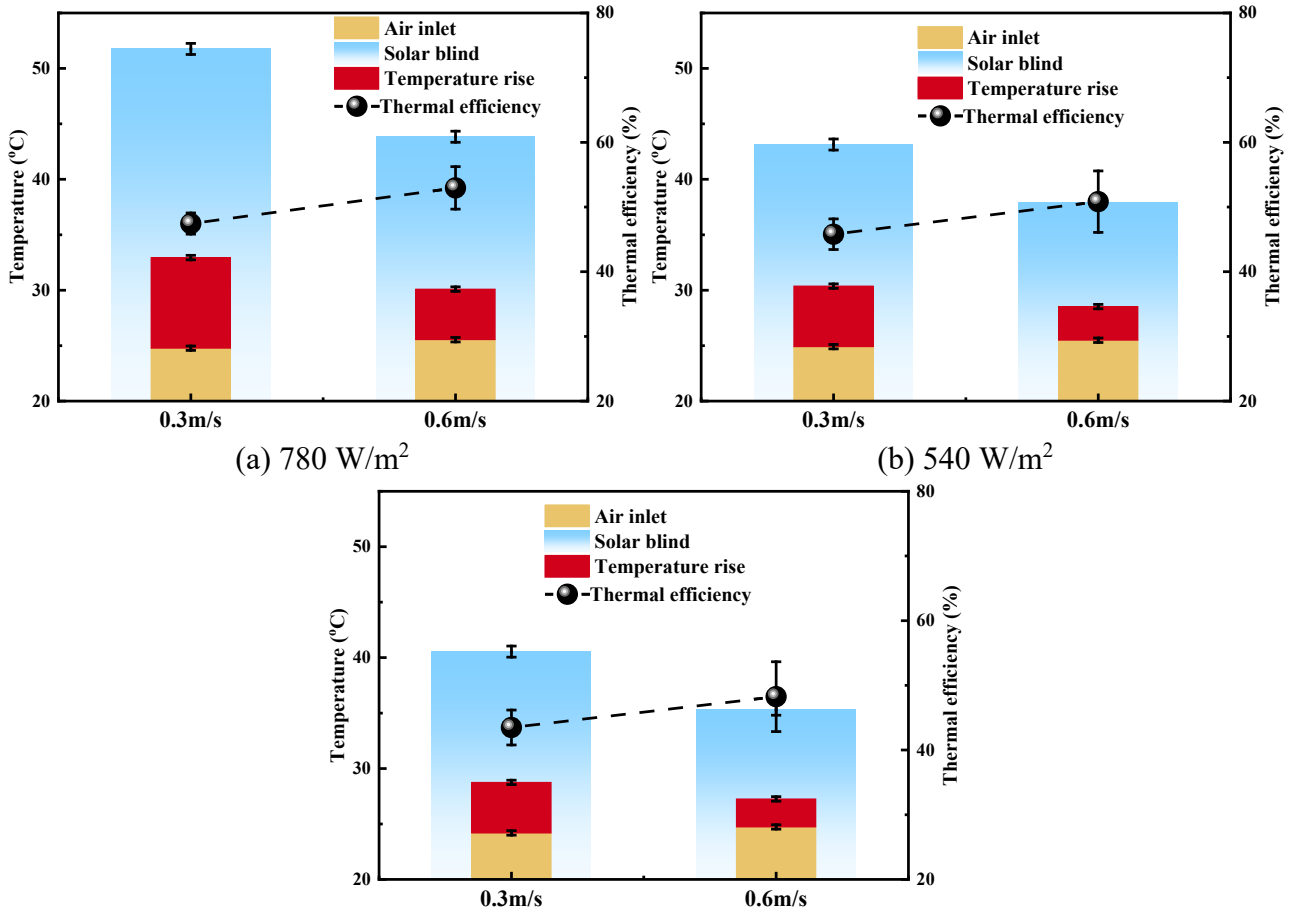

(a) 780 W/m^2 (b) 540 W/m^2

(c) 475 W/m^2

Fig. 9 Experimental results of FISC system under air heating mode

When operating under water heating mode, the experimental results of temperature variation are shown in Fig. 10. The temperature of the solar blinds remains higher than that of the water in the tank.

However, due to the higher heat transfer performance of water compared to air, the temperature difference between the solar blinds and water is lower than the temperature difference between the solar blinds and cavity air under air heating mode. Examining the profiles of the water temperature in tank, it is found that the increase rate of temperature gradually slows down. This is because the higher temperature of the inlet water reduces the heat transfer between the water and solar blinds. The experimental results of the average thermal efficiencies are shown in Fig 11. The initial temperatures of the water tank for the three irradiations are 25.8℃. The maximum temperature rises under the three irradiations are 24.8℃, 18.9℃, and 15.8℃, respectively. The average thermal efficiencies under the three irradiations are 38.6%, 39.7%, and 39.8%, respectively.

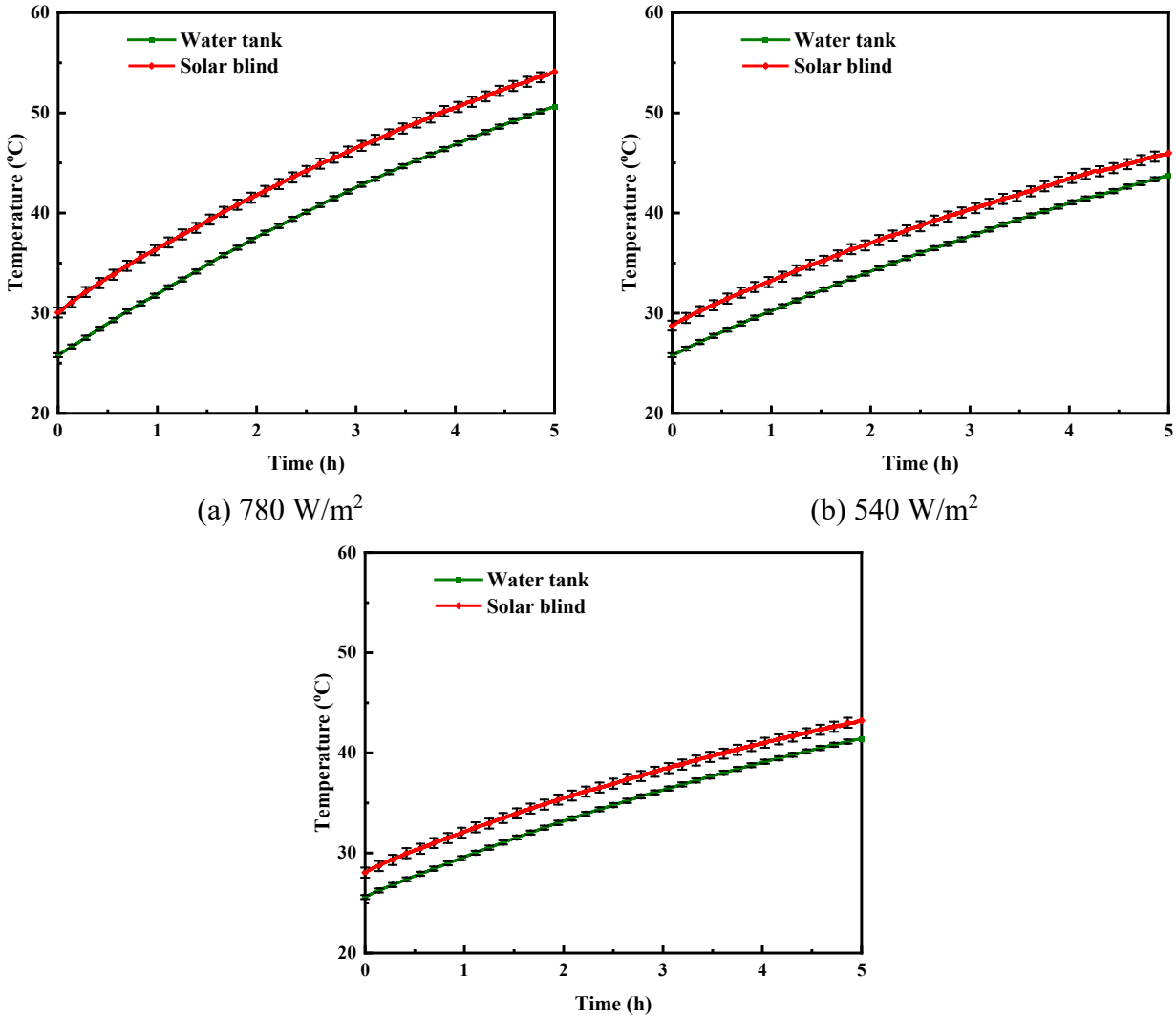

(a) 780 W/m^2 (b) 540 W/m^2

(c) 475 W/m^2

Fig. 10 Temperature variation under water heating mode

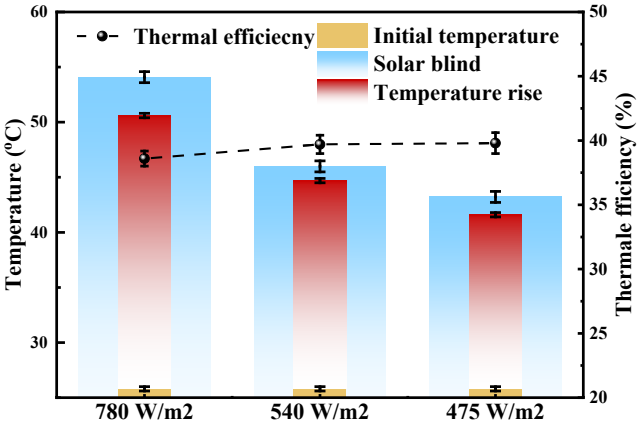

Fig. 11 Temperature variation under water heating mode

4.1.3. Model validation

To validate the accuracy of the mathematical model of the FISC system, an additional experiment was conducted on the unstable state. The experiment lasted for a total of 16 hours, during which the water pump and a fan were continuously operational. For the first 4.5 hours, all lamps of the solar simulators were turned on, and for the remaining time, all lamps were turned off. This experiment involved dynamic heat transfer under unsteady conditions and the interaction between air and water heating. Hence, the validation of these experimental data is more effective in confirming whether the model can precisely predict the heat transfer behavior of the FISC system. To quantify the simulation error, the coefficient of root-mean-square error (Cv(RMSE)) and mean bias error (MBE) are used as metrics for evaluation. The equations for calculating these two metrics are provided as follows:

$$Cv(RMSE) = \frac{\sqrt{\Sigma_{i=1}^{N}(S_i - M_i)^2/N}}{\Sigma_{i=1}^{N} M_i/N} \tag{40}$$

$$MBE = \frac{\Sigma_{i=1}^{N}(S_i - M_i)}{\Sigma_{i=1}^{N} M_i} \tag{41}$$

where, S and M represent the simulated and measured values. N is the number of the validated data. According to ASHRAE Guideline 14, the accuracy of the model is considered to be acceptable when Cv(RMSE) and MBE are lower than 30% and 10%, respectively [49].

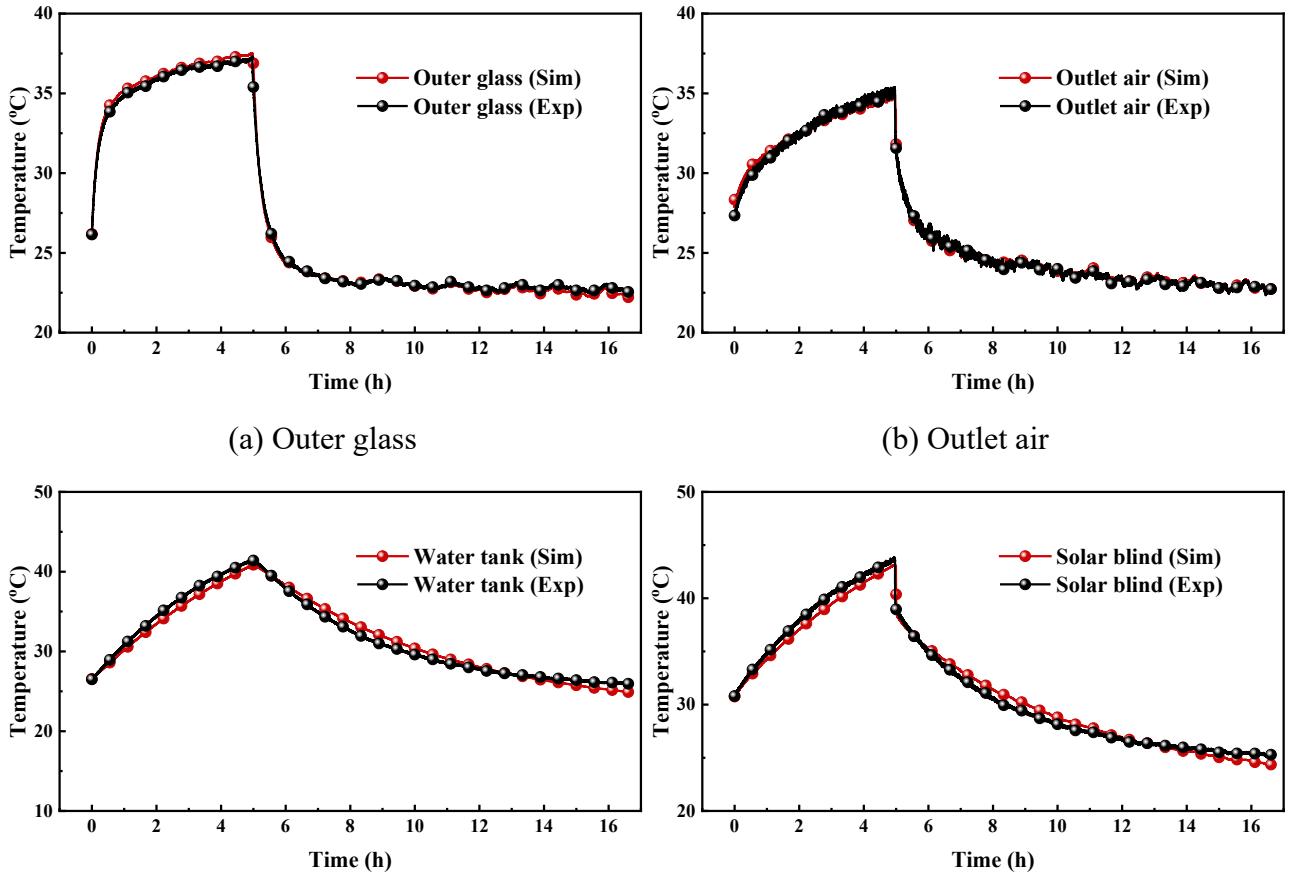

(a) Outer glass (b) Outlet air

(c) Water tank (d) Solar blind

Fig. 12 Comparison between the simulation results and experiment data

The comparison between the simulation results and experiment data is presented in Fig 12. It can be observed that the simulation results closely match the experimental data. When the lamps are turned on, the temperatures of all components increase rapidly. After being exposed to irradiation for 4.5 hours, the temperature variation of all components approaches a steady state. When the lamps are turned off, the temperature of the outer glass rapidly drops to the surrounding air temperature. The error analysis indicates that the coefficient of root-mean-square error (Cv(RMSE)) values for the outer glass, outlet air, water tank, and solar blind are 0.82%, 0.92%, 2.35%, and 1.99%, respectively. The mean bias error (MBE) values for these components are -0.06%, 0.01%, 0.21%, and 0.24%, respectively. Thus, the developed mathematical model can reliably simulate the thermal behavior of the FISC system.

4.2. Sensitivity analysis

The thermal performance of fenestration systems is generally evaluated based on solar heat gain and thermal insulation [42]. The thermal insulation performance is indicated by the U value, which represents the overall heat transfer coefficient of the fenestration system. The U value is the ratio of the heat loss through the fenestration system at night to the temperature difference between the indoor and outdoor environments. On the other hand, solar heat gain is quantified by the solar heat gain coefficient (SHGC), which represents the fraction of solar radiation entering the room through the fenestrations. It is calculated as the ratio of the solar heat gain to the irradiation incident on the fenestration systems. The definition equations of U value and SHGC are written as [50]:

$$U = \frac{Q_c + Q_r}{T_{out} - T_{in}} \tag{42}$$

$$SHGC = \frac{Q_t + Q_c + Q_r}{Q_s} \tag{43}$$

where, Q_c and Q_r are the indoor convective and radiative heat gain through the fenestrations (W/m^2). Q_s and Q_t are the solar radiation incident on the fenestration and the solar radiation penetrating the fenestration (W/m^2). T_{out} and T_{in} are the outdoor and indoor temperatures (℃).

This section utilizes the validated simulation model to analyze the impact of the slat angle, blind position, and air depth on the thermal performance of the FISC system. In addition to analyzing the thermal efficiency of the system, this section also provides a detailed analysis of the SHGC and U values. The SHGC and U value of the double clear glazing (DCG), which are constructed by the same glasses of the FISC system and a 12 mm air gap, are calculated using the *WINDOW* software [51] for comparison. The calculation is performed under the boundary conditions specified by the CEN environmental conditions in *WINDOW* software, which are the standard condition used for calculating the thermal performance of fenestrations. During the analysis process, the air velocity and water flow rate are 0.3 m/s and 15 min/L. When evaluating the thermal performance under water heating mode, the water inlet temperature is assumed to be 28℃.

4.2.1. Slat angle

The thermal performance of the FISC system for different slat angles is presented in Fig. 13. It is observed that the thermal efficiency for air heating increases as the slat angle increases. This is because a larger slat angle results in an increased surface area for absorbing irradiation by the solar blind. However, as the slat angle increases, the heat loss to the outdoors also increases due to the higher temperature of the solar blind. Consequently, the SHGC decreases. Compared to the DCG, the FISC system consistently exhibits higher SHGC values at different slat angles, indicating enhanced indoor heat gain. In the water heating mode, the thermal efficiency of the FISC system also increases with the slat angle. However, the SHGC of the FISC system decreases significantly as the slat angle increases. This is because that the solar heat gain of water heating mode mainly relies on solar transmittance. Compared to the DCG, the FISC system demonstrates lower SHGC values at different slat angles. The U values of the FISC system decrease with the increase of the slat angle. This is because larger slat angles decrease the view factor between the inner and outer glazing, resulting in reduced radiative heat transfer coefficients between these two layers. Compared to the DCG, the FISC system exhibits lower U values at different slat angles. Thus, the proposed system improves the thermal insulation performance of the fenestration system.

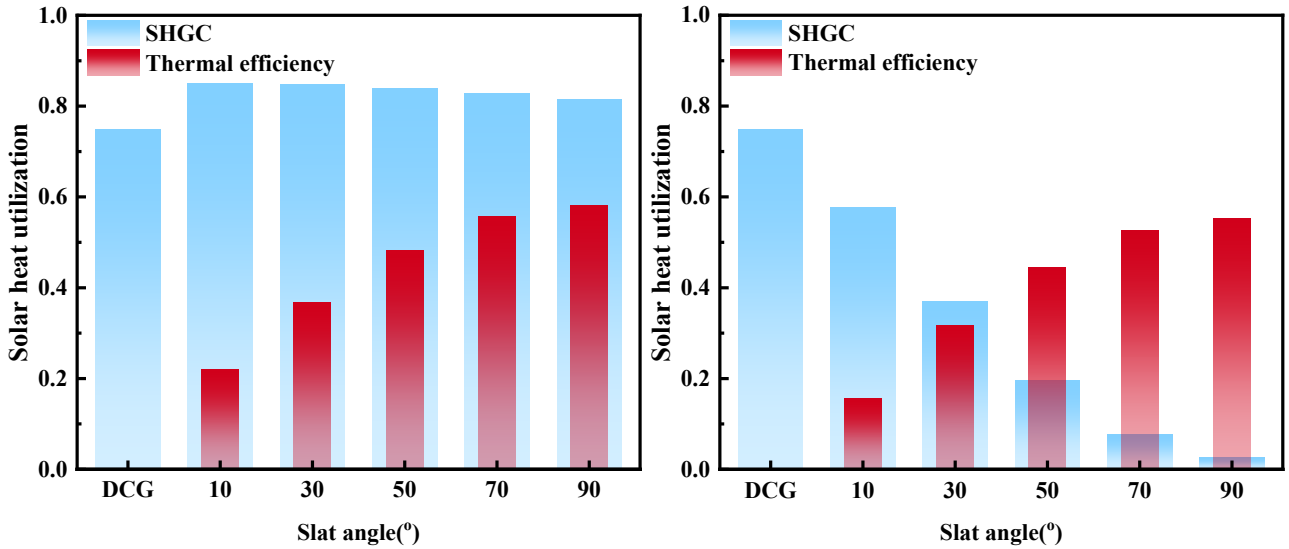

(a) Air heating mode (b) Water heating mode

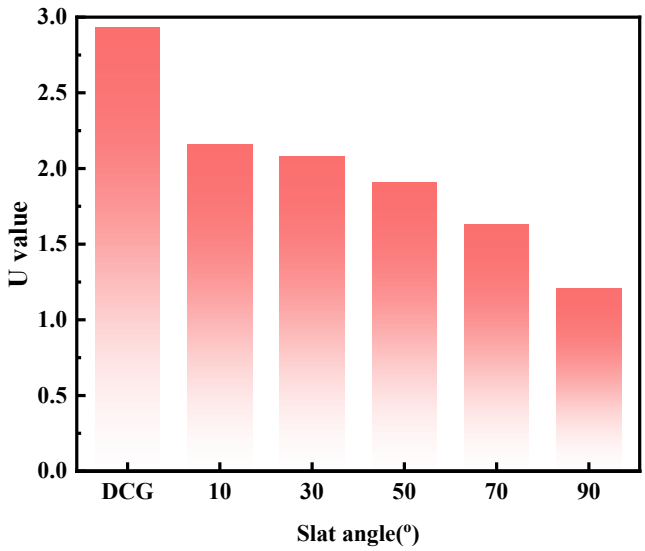

(c) Thermal insulation

Fig. 13 The thermal performance of the FISC system for different slat angles

4.2.2. Blind position

The thermal performance of the FISC system for different blind positions is illustrated in Fig. 14 In this analysis, the blind position is defined as the distance between the solar blind and the outer glazing. As the solar blinds are moved from the outer side to the inner side, the air heating efficiency initially decreases, then reaches a minimum, and finally increases. When the blinds are positioned in the middle of the air cavity, the thermal efficiency is the lowest. The trend of the SHGC follows the same pattern as the thermal efficiency, since the solar transmittance remains constant for different blind positions. This indicates that locating the solar blinds away from the middle position improves the thermal performance of the system. This is because a smaller distance between the air flow channel and the solar blind enhances convective heat transfer between the blind and the cavity air. In contrast to the air heating mode, the blind position has minimal impact on the solar heat utilization performance and thermal insulation properties in the water heating mode. A comparison with the DCG reveals that the FISC system exhibits a higher SHGC in the air heating mode, a lower SHGC in the water heating mode, and improved thermal insulation performance at night.

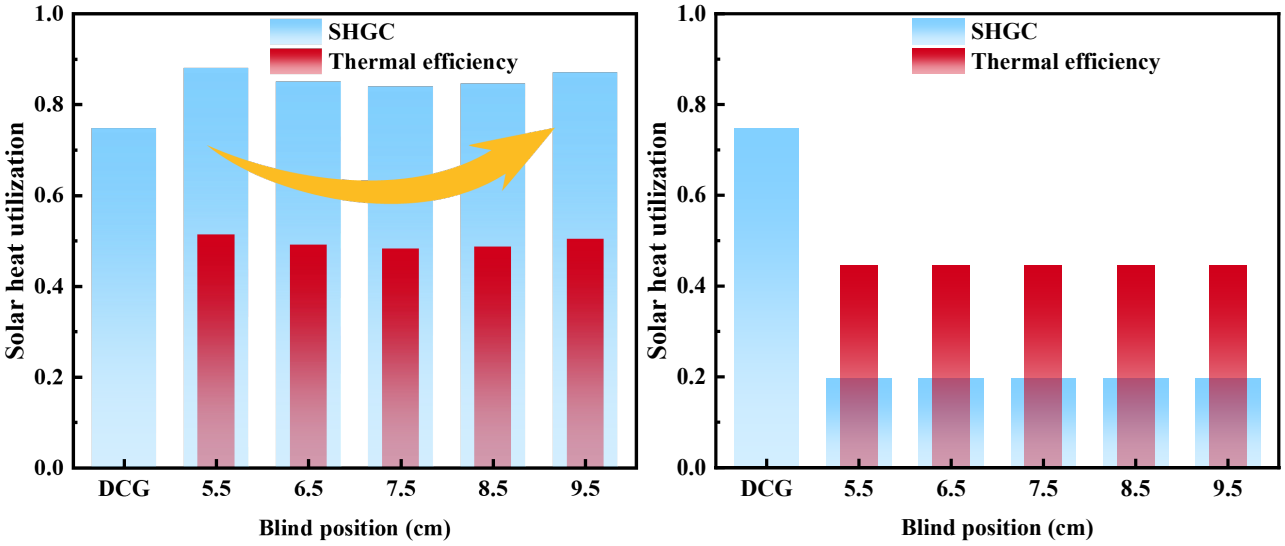

(a) Air heating mode

(b) Water heating mode

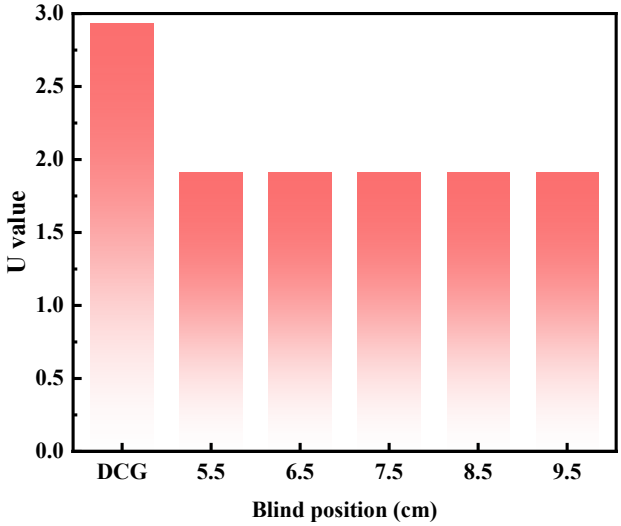

(c) Thermal insulation

Fig. 14 The thermal performance of the FISC system for different blind position

4.2.3. Cavity depth

The thermal performance of the FISC system for different air depths is presented in Fig. 15. When the system operates in air heating mode, a larger cavity depth results in a higher mass flow rate of cavity air, leading to more heat being carried away from the solar blind. As shown in Fig. 15 (a), both the thermal efficiency and SHGC increase with the increase of cavity depth. However, since the temperature of the solar blind primarily depends on the inlet water temperature, the thermal

performance of the FISC system remains relatively unaffected by the cavity depth. Increasing the depth of the air cavity generally leads to a lower convective heat transfer coefficient in the air cavity, thus improving the thermal insulation performance. However, as shown in Fig. 15 (c), the improvement in insulation performance is somewhat limited. Consistent with the findings from the previous subsections, the SHGC of the FISC system in the air heating mode is higher than that of the DCG, while in the water heating mode, it is lower. The proposed system demonstrates better insulation performance than the DCG across all cavity depths.

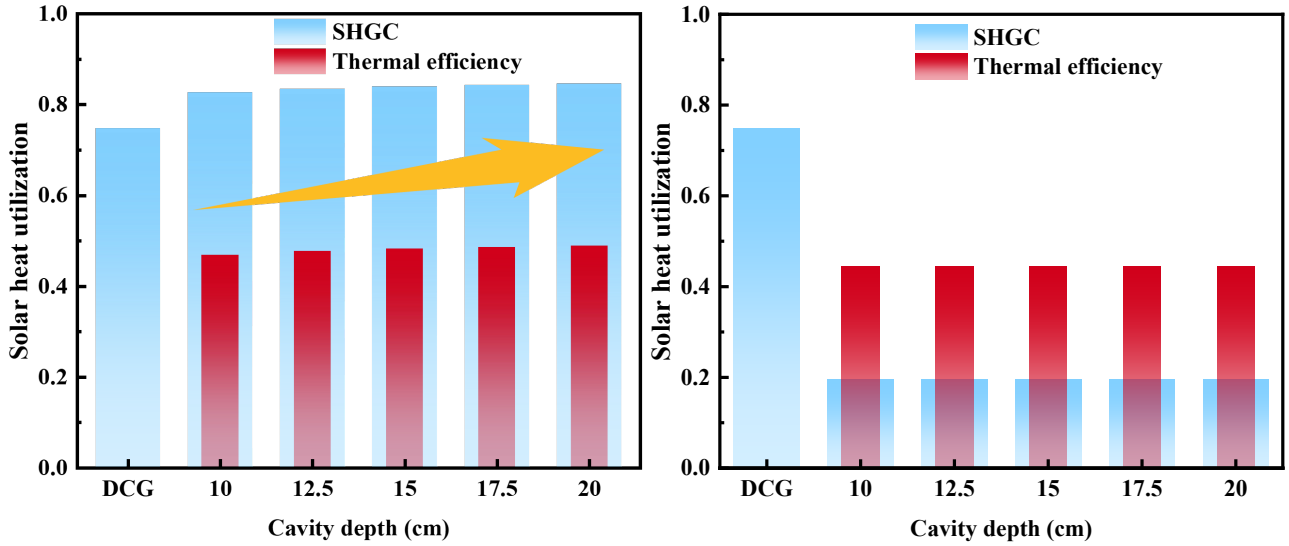

(a) Air heating mode (b) Water heating mode

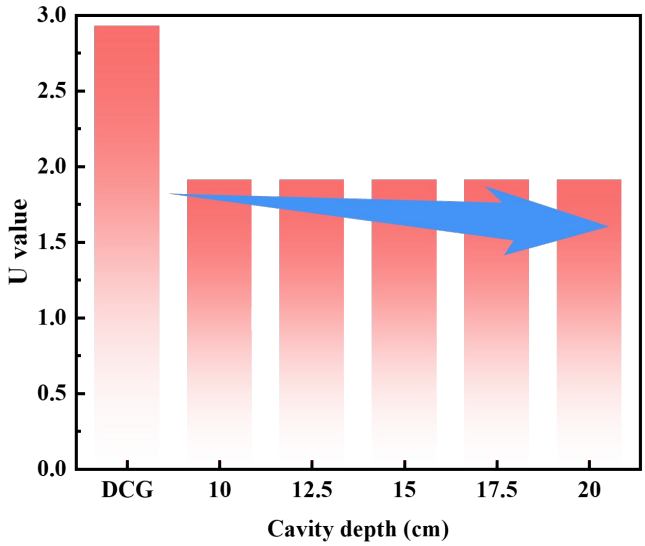

(c) Thermal insulation

Fig. 15 The thermal performance of the FISC system for different air depth

4.2.4. Discussion on the structural parameter

The above subsections provide a nuanced understanding of how various factors influence the thermal performance of the FISC system. By combining all the studied parameters, the optimal configuration of the FISC system is obtained in terms of thermal efficiency and thermal insulation performance, as listed in Table 4. It can be seen that increasing the slat angle is beneficial for the thermal performance. Moreover, under the CEN environmental conditions, positioning the solar blind away from the inner glass help improve air thermal efficiency, while placing it closer to the inner glazing help improve water heating efficiency. However, some practical considerations and challenges should be noted when adjusting these parameters in real-world applications. Firstly, the large slat angle generally reduces the amount of natural light entering the room and obstructs the view of indoor people. Thus, the engineers should take into account the lighting requirements of the building itself, as well as other natural lighting installations (windows, skylights, light guides, etc.) and the subjective perception of the people when deciding on the slat angle. It is worth mentioning that the development of systems with rotating blind will contribute to the performance and promotion of the system. Secondly, adjusting the blind position and cavity depth affects the structural stability of the system and needs to be handled with care. For instance, blind positioned too close to the glass may interfere with the installation of the fan and header pipe. Lastly, the results listed in Table 4 are calculated based on the CEN environmental conditions. In fact, the optimal configuration in different boundary conditions is different. The engineer should simulate it based on the local design conditions of fenestration system before making decision.

Table 4 The optimal configuration of the FISC system under CEN environmental conditions

	Air heating efficiency	Water heating efficiency	Thermal insulation
Slat angle	90°	90°	90°
Blind position	15.5 cm	4.5 cm	10 cm
Cavity depth	0.2 m	0.15 m	0.2 m

4.3. Energy-saving and economic assessment

In this section, the energy-saving potential and economics of the FISC system is predicted. For the case study, three distinct building types developed by the U.S. Department of Energy are selected: a quick-service restaurant for commercial buildings, a factory for industry buildings, and an apartment for residential buildings. The building layouts are depicted in Fig. 16. Detailed information regarding the building dimensions and wall materials can be found in the Reference [52]. As shown in Fig. 16, based on the window sizes of the buildings, six, four, and two FISC systems were installed on the south-facing windows of the three types of buildings studied. Each system maintained the same size and physical parameters as in the experimental setup. In this case study, it was assumed that the air velocity of the fan was 0.3 m/s (rated power of 8 W) and the water flow rate of the pump was 15 L/min (rated power of 46 W), which aligns with the experimental setup. The benchmark for comparison was the DCG, commonly used in buildings. While the FISC system is designed for cold winter and hot summer region, this section extends its analysis to evaluate energy-saving potential in subtropical, tropical, and temperate regions, represented respectively by Hefei (31.9 N, 113.7 E), Haikou (20.03 N, 110.35 E), and Harbin (45.75 N, 126.77 E). Hefei is a typical region with cold winter and hot summer, situated in the mid-eastern part of China. The heating period extends from January to March and from November to December, while the cooling period is from May to September. In Hefei, the air heating mode of the proposed system is activated in heating seasons, while its water heating mode is used in other seasons. Unlike Hefei, both Haikou and Harbin experience less distinct seasonal variations. Haikou, situated in the south of China, has no heating requirements. Thus, only the water heating mode of the FISC system is utilized throughout the year. In contrast, Harbin, in the northern part of China with low ambient temperatures and negligible cooling needs, employs only the air heating mode.

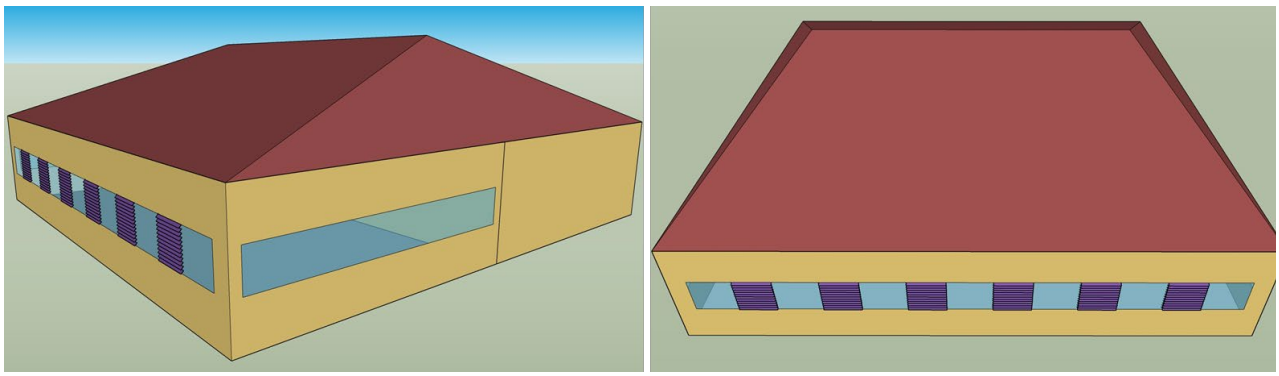

(a) Commercial building

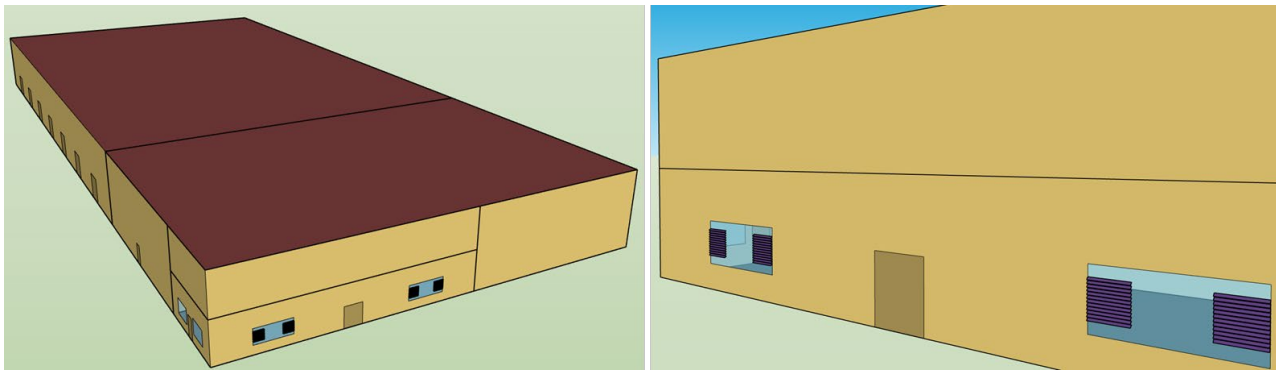

(b) Industry building

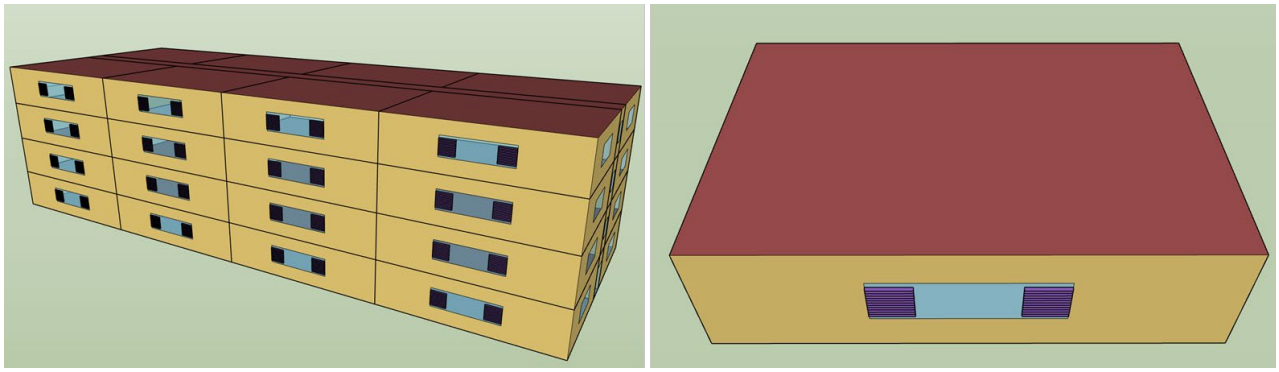

(c) Residential building

Fig. 16 The sketch of the reference building in case study

In this study, the energy-saving potential of the case study was predicted using the TRNSYS 18.0 platform. The component layout and data flow of the case study within the TRNSYS platform are illustrated in Fig. 17. The thermal balance of the building was modeled using Type 56. The cooling and heating set temperatures, as per the GB 19576-2019 standard in China, were set to 24℃ and 20℃, respectively. Type 158 was utilized to model the water tank, while Type 138 represented the auxiliary heater used to heat the water to the desired temperature. For the case study, it was assumed that the

volume of water tank for commercial, industry, and residential buildings were respectively 500 L, 350L, and 150 L, while the desired water use temperature was 45℃. The flow rate of water use remained constant throughout the water use time and the daily hot water demand is equal to the capacity of the tank. The mathematical models of the FISC system programmed using Matlab code was imported into the TRNSYS platform via Type 155. The indoor temperature, provided by Type 56, and the water inlet temperature, provided by Type 158, were inputted into Type 155 as boundary conditions. The indoor heat gain and water outlet temperature calculated by Type 155 were then fed into Type 56 and Type 158, respectively. The meteorological data of the typical meteorological year in the Hefei, Haikou, and Harbin were obtained through Type15 and passed to Type 56, Type 155, and Type 158. According to the usual user habits, the building's air conditioning time for three type building was set as 8:00~23:00, 8:00~17:00, and 0:00~24:00, while the water use time was set as 8:00~23:00, 8:00~17:00, and 8:00~22:00.

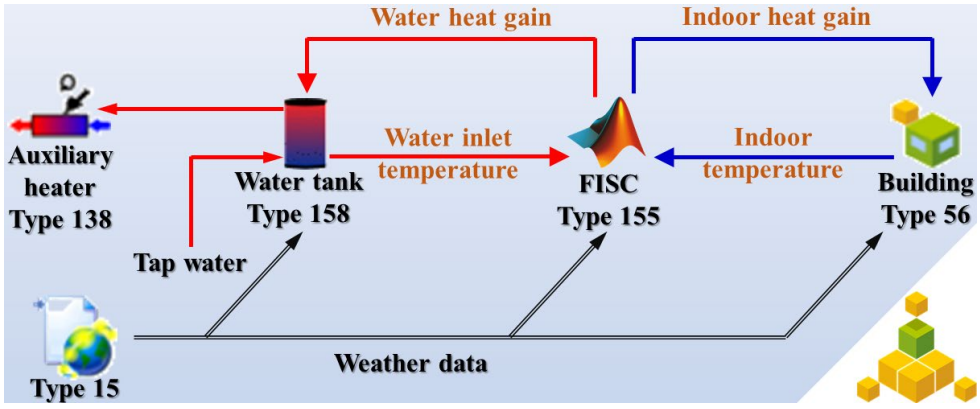

Fig. 17 The component layout and data flow of the studied case in TRNSYS platform

The annual energy saving of FISC system in different climate regions is shown in Fig. 18. Regardless of the region, the system offers varying degrees of energy savings compared to DCG. While producing the hot water, the air heating mode can reduce indoor space heating load and the water heating mode can reduce space cooling load. The reason of reducing heating load is that the FISC system have a higher solar heat gain coefficient and better thermal insulation, as shown in the results in 4.2 section. The main reason of reducing cooling load is that the shading of solar blind and the cooling of water pipe. This calculation result demonstrates the applicability of the system in different seasons. In Harbin, where only the air heating mode is used, no energy savings for water

heating are generated. The energy savings of the FISC system are similar across all types of buildings. Taking commercial buildings as an example. the total energy savings of each FISC system are approximately 225 kWh, 210 kWh, and 53 kWh in Hefei, Haikou, and Harbin.

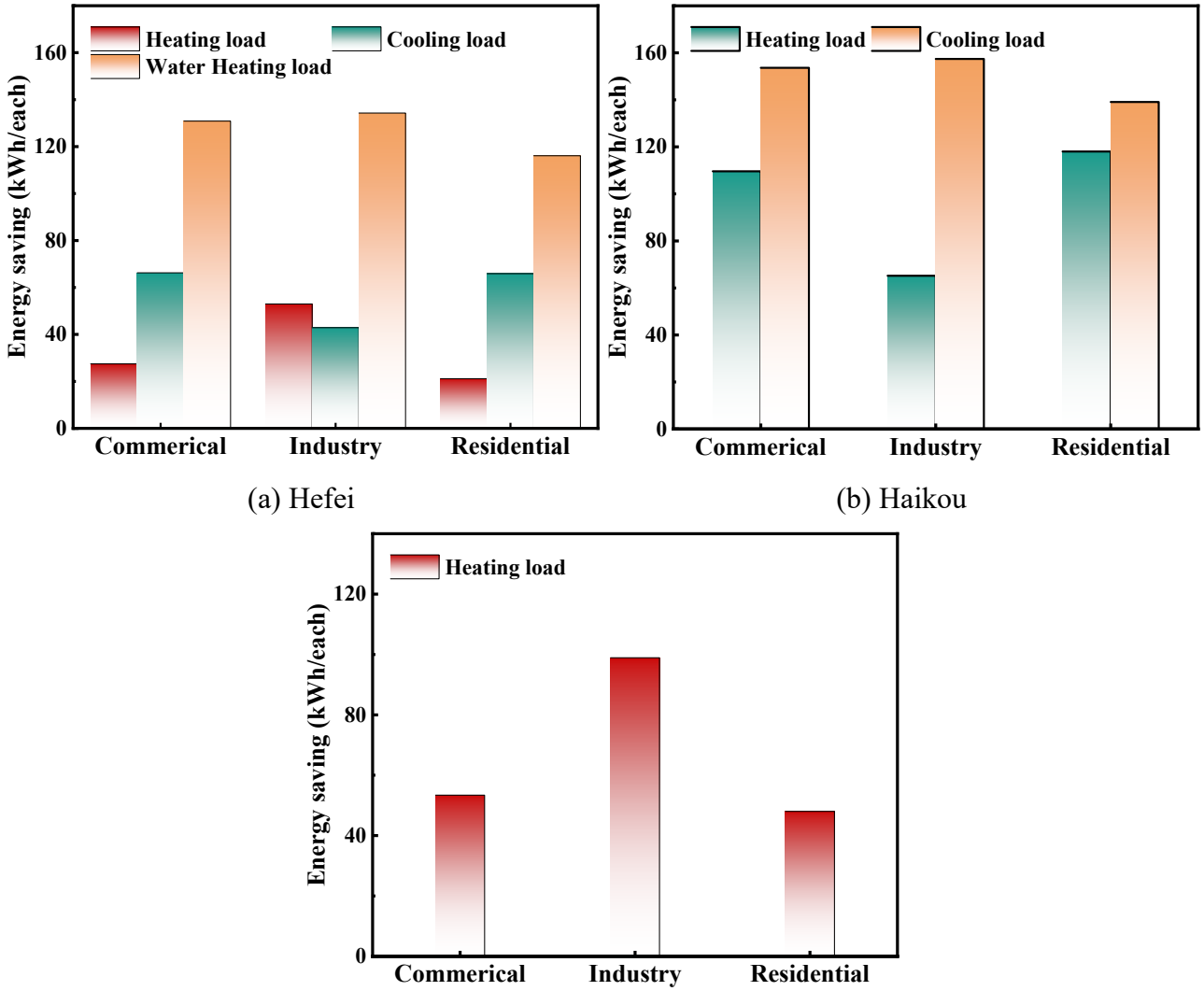

(a) Hefei (b) Haikou

(c) Harbin

Fig. 18 The annual energy saving of FISC system in different climate regions

The economic feasibility of the proposed FISC system was analyzed based on the return on investment (ROI). The ROI is calculated as [53]:

$$\mathrm{ROI} = \frac{\text{Benefits} - \text{Operation cost}}{\text{Investment cost}} \tag{44}$$

where, the Benefits represent the economic benefits of the system in operation compared to the DCG. The Operation cost is the electricity costs during the operation of fans and water pumps. The Investment cost is the additional material and product cost of the FISC system compared to the

DCG. The economic benefits of the system are calculated by equating energy savings to the operation cost of traditional heating/cooling equipment. It was assumed that an air source heat pump (COP=2.9) was used for space cooling, an electric heating coil (COP=0.9) was adopted for space heating, while the domestic hot water was heated by the resistance wire with the efficiency of 1.0. The tariff is 0.8 RMB/kWh for commercial and industry buildings and 0.6 RMB/kWh for residential buildings. The FISC system is relatively cost-effective, comprising glass, copper tubes, and solar absorber panel. In contrast to the DCG, the additional components of the FISC system are the solar blind group, fan, and water pump. The costs of inner and outer glass are not considered as they are the essential elements for the DCG. Based on data collected during the fabrication process, the price of copper pipe is 7 RMB/m and the price of solar absorber panel is 60 RMB/m^2. The total additional material costs of the FISC system were estimated to be approximately 165 RMB/each. The costs of the fan and water pump are 35 RMB and 82 RMB, respectively.

The calculated results of the annual ROIs of the FISC system are listed in Table 5. It can be seen that the ROIs in Hefei and Haikou are similar while the value in Harbin is significantly lower. The reason for this discrepancy is that when the system is employed in Harbin, the water heating function is omitted. Consequently, the system can only realize the benefits of the air-conditioning load and not the water heating load. In Haikou, even though the air heating function is not utilized, the economic return of the system is still significant. Thus, it can be deduced that the practical implementation of the FISC is viable in subtropical and tropical regions, while it is less economically efficient in temperate regions. The annual ROI of the FISC system in Hefei and Haikou ranges from 0.30 to 0.52. Consequently, the payback period for implementing the system in these two regions is estimated to be around 2 to 4 years. The life cycle of the FISC system is 25 years. In the case of Hefei, for example, the total cost of the system over the life cycle, including the investment cost and operation cost, is compared to the additional cost of the various traditional heating/cooling equipment that would be required without the assistance of the FISC system. The results are listed in Table 6. It can be observed that the FISC system offers the highest benefit in terms of water heating and the lowest benefit in terms of cooling load reduction. The proposed system can simultaneously offset the energy consumption of three compared traditional equipment. Upon summation, it is evident that the each

FISC system can lead to the cost reductions of 2942 RMB, 3419 RMB, and 1808 RMB for commercial, industrial, and residential buildings, respectively.

Table 5 The annual ROIs of the FISC system

	Commercial building	Industry building	Residential building
Hefei	0.46	0.52	0.30
Harbin	0.10	0.23	0.06
Haikou	0.45	0.42	0.31

Table 6 Comparison of total cost with the traditional heating/cooling equipment (RMB)

	Commercial building	Industry building	Residential building
Air source heat pump	456	296	341
Electric heating coil	610	1177	353
Resistance wire	2618	2686	1741
FISC system	742	740	627

4.4. Comparison with systems in published literature

To underscore the novelty of this study, a comparative analysis is conducted between the FISC system and other solar fenestration systems in the published literature, focusing on functions and performance indicators. The outcomes of this comparison are presented in Table 7. The air heating function of solar fenestration systems aims at augmenting the SHGC to elevate indoor temperatures. For instance, the triple-glazed airflow window in Reference [15] achieved a SHGC of up to 0.87. However, such solar fenestration designs are more suitable for deployment in winter, as they tend to escalate cooling energy consumption in summer. Conversely, the solar fenestration systems incorporating water flow functions primarily intend to decrease the SHGC and provide shading effects. These designs are less applicable in winter or cold climates due to higher building heating loads resulting from lower SHGC and the risk of freezing waterways. Scrutinizing the fenestration systems presented in the table reveals a scarcity of designs in the published literature that simultaneously possess both air and water heating functions. This limitation renders such systems less adaptable to seasonal variations and less suitable for regions characterized by cold winters and

hot summers. On the contrary, the FISC system exhibits a distinctive capability to dynamically adjust the SHGC through mode switching. Consequently, compared with the previous fenestrations, the proposed FISC system emerges as a promising solution for application in subtropical regions. Moreover, in terms of thermal efficiency and U values, the FISC system proves competitive when juxtaposed against other fenestration systems in the literature. The windows in Reference [15] had three panes of glass, whereas the inner glazing of the windows in reference [16] was low-e glass, resulting in a lower U-value. If the inner glazing of the FISC system is replaced with double-skin glass or low-e glass, the thermal insulation performance of the system at night will be further enhanced. Notably, the ongoing emergence of Photovoltaic/Thermal fenestrations [29, 54] bears consideration. If the PV cells are incorporated onto the blinds of the proposed FISC system, an additional function of power generation is yielded and the solar energy utilization efficiency can be further increased.

Table 7 Comparison with other solar fenestration systems in published literature

System	Functions	Thermal efficiency	SHGC	U value
Exhaust air window with blinds [30]	Shading, thermal insulation	\	0.22	1.57
Blind window solar air collector [28]	Shading, air heating	46%	\	\
PV/T collector for fenestration [29]	PV output, air heating	32%	\	\
Triple-glazed airflow window [15]	Air heating, thermal insulation	\	0.87	0.1
Supply-air double windows [16]	Air heating, thermal insulation	\	\	1.46
Water heating smart window [25]	Shading, water heating	42%	\	\
Hybrid solar window [31]	Shading, water heating	21~26%	0.43	2.0
Window with pipes embedded in blinds [32]	Shading, water heating	60%	0.13	\
Triple-glazed water flow window [55]	Shading, water heating	31%	\	\
Double-glazed water flow window [17]	Shading, water heating	\	0.23	3
PV ventilated blind window [54]	PV output, shading	\	0.20	3.30
Present work	Shading, air heating, water heating, thermal insulation	40%~50% for air heating, 39% for water heating	0.84 for air heating, 0.19 for water heating	1.91

5. Conclusion

This study presented a novel building fenestration-integrated solar collector aimed at enhancing solar energy utilization and seasonal adaptability. The system incorporates a solar blind positioned within the cavity of a double-skin ventilation glazing, with water pipes welded behind the solar blind. In winter, the exchange of cavity air with indoor air allows the recovery of heat from the solar blind to increase indoor temperature. During summer and other seasons, the tap water is induced into the water pipe for cooling, thereby reducing indoor heat gain, while the heat on solar blind is recovered to produce hot water. By adapting to different work modes based on the season, the proposed system enables the year-round solar utilization. To evaluate the thermal performance, a prototype of the proposed system was fabricated and tested under various work modes. Additionally, a mathematical model was developed and validated using the collected experimental data. The impact of structural parameters on system performance was examined, followed by the prediction of energy-saving potential and economic for various type of buildings. The key findings are summarized as follows:

(1) In air heating mode, the thermal efficiency of the proposed system increased with irradiation and air velocity, ranging around 40~50%. In water heating mode, the thermal efficiency remained relatively constant across different irradiation levels. The average thermal efficiency for water heating was around 39%.

(2) The developed mathematical model could accurately capture the thermal behavior of the proposed system under the dynamic conditions. The comparison between the simulation results and experimental data indicated that the coefficient of root-mean-square error values were lower than 2.35%, and the mean bias error values were not larger than 0.24%.

(3) Increasing the slat angle improved thermal efficiency and thermal insulation performance while decreasing SHGC of the proposed system. Moving the solar blinds away from the middle position and increasing the cavity depth could improve the thermal performance under air heating mode. The influence of blind position and cavity depth under water heating mode was negligible.

(4) The proposed system exhibited significant potential for energy savings in commercial, industrial,

and residential buildings. The economic analysis demonstrated its favorable economic performance in both subtropical and tropical regions, with a projected payback period of 2 to 4 years. However, in temperate regions, the economic performance was comparatively less favorable.

Overall, this study developed and tested a novel building fenestration-integrated solar collector system and demonstrated its energy-saving potential and improved thermal performance. The findings contribute to the field of sustainable building design and provide valuable insights for optimizing solar energy utilization in regions with diverse seasonal thermal demands.

6. Acknowledgement

This work was supported by the research funding of the Joint Postdoc Scheme with Non-local Institutions of The Hong Kong Polytechnic University.

References

[1] International Energy Agency, Heating, (2022).
[2] S. Gorjian, H. Ebadi, F. Calise, A. Shukla, C. Ingrao, A review on recent advancements in performance enhancement techniques for low-temperature solar collectors, Energy Conversion and Management 222 (2020).
[3] M.S. Buker, S.B. Riffat, Building integrated solar thermal collectors – A review, Renewable and Sustainable Energy Reviews 51 (2015) 327-346.
[4] X. Su, L. Zhang, Y. Luo, Z. Liu, Energy performance of a reversible window integrated with photovoltaic blinds in Harbin, Building and Environment 213 (2022).
[5] K. Pelletier, C. Wood, J. Calautit, Y. Wu, The viability of double-skin façade systems in the 21st century: A systematic review and meta-analysis of the nexus of factors affecting ventilation and thermal performance, and building integration, Building and Environment 228 (2023).
[6] Y. Tang, J. Ji, C. Wang, H. Xie, W. Ke, Combining photovoltaic double-glazing curtain wall cooling and supply air reheating of an air-conditioning system: Energy-saving potential investigation, Energy Conversion and Management 269 (2022).
[7] Y. Etzion, E.J.B. Erell, Environment, Controlling the transmission of radiant energy through windows: a novel ventilated reversible glazing system, Building and Environment 35(5) (2000) 433-444.
[8] E. Erell, Y. Etzion, N. Carlstrom, M. Sandberg, J. Molina, I. Maestre, E. Maldonado, V. Leal, O. Gutschker, "SOLVENT": development of a reversible solar-screen glazing system, Energy and Buildings 36(5) (2004) 467-480.
[9] T.-t. Chow, Z. Lin, K.-f. Fong, L.-s. Chan, M.-m. He, Thermal performance of natural airflow window in subtropical and temperate climate zones – A comparative study, Energy Conversion and Management 50(8) (2009) 1884-1890.

[10] C. Wang, J. Ji, M.M. Uddin, B. Yu, Z. Song, The study of a double-skin ventilated window integrated with CdTe cells in a rural building, Energy 215 (2021).
[11] W. Guo, L. Kong, T. Chow, C. Li, Q. Zhu, Z. Qiu, L. Li, Y. Wang, S.B. Riffat, Energy performance of photovoltaic (PV) windows under typical climates of China in terms of transmittance and orientation, Energy 213 (2020).
[12] P. Baker, M. McEvoy, Test cell analysis of the use of a supply air window as a passive solar component, Solar Energy 69(2) (2000) 113-130.
[13] J.S. Carlos, H. Corvacho, P.D. Silva, J.P. Castro-Gomes, Heat recovery versus solar collection in a ventilated double window, Applied Thermal Engineering 37 (2012) 258-266.
[14] J.S. Carlos, Optimizing the ventilated double window for solar collection, Solar Energy 150 (2017) 454-462.
[15] G. Michaux, R. Greffet, P. Salagnac, J.-B. Ridoret, Modelling of an airflow window and numerical investigation of its thermal performances by comparison to conventional double and triple-glazed windows, Applied Energy 242 (2019) 27-45.
[16] Y. Huang, M. El Mankibi, R. Cantin, Thermal performance characterization of supply-air double windows: A new guarded hot box protocol and numerical modelization, Energy and Buildings 287 (2023).
[17] L.J. Claros-Marfil, V. Zetola, J.F. Padial, B. Lauret, Experimental-simulation methodology for estimation of thermal parameters of adaptive facades in mild climate conditions: A water-flow glazing case study, Journal of Building Engineering 45 (2022).
[18] T.-T. Chow, C. Li, Z. Lin, The function of solar absorbing window as water-heating device, Building and Environment 46(4) (2011) 955-960.
[19] T.-T. Chow, C. Li, Liquid-filled solar glazing design for buoyant water-flow, Building and Environment 60 (2013) 45-55.
[20] T.T. Chow, Y. Lyu, Effect of design configurations on water flow window performance, Solar Energy 155 (2017) 354-362.
[21] Y.-L. Lyu, T.-T. Chow, J.-L. Wang, Numerical prediction of thermal performance of liquid-flow window in different climates with anti-freeze, Energy 157 (2018) 412-423.
[22] Y.-L. Lyu, W.-J. Liu, H. Su, X. Wu, Numerical analysis on the advantages of evacuated gap insulation of vacuum-water flow window in building energy saving under various climates, Energy 175 (2019) 353-364.
[23] C. Li, H. Tang, Evaluation on year-round performance of double-circulation water-flow window, Renewable Energy 150 (2020) 176-190.
[24] M. Gutai, A.G. Kheybari, Energy consumption of water-filled glass (WFG) hybrid building envelope, Energy and Buildings 218 (2020).
[25] L. Wang, X. Jiao, D. Chen, T. Wang, A Solar Water-Heating Smart Window by Integration of the Water Flow System and the Electrochromic Window Based on Reversible Metal Electrodeposition, Advanced Science 9(6) (2022) e2104121.
[26] M. Konstantoglou, A. Tsangrassoulis, Dynamic operation of daylighting and shading systems: A literature review, Renewable and Sustainable Energy Reviews 60 (2016) 268-283.
[27] N. Onur, M. Sivrioğlu, O. Turgut, An experimental study on air window collector having a vertical blind for active solar heating, Solar energy 57(5) (1996) 375-380.
[28] N.I. Dawood, J.M. Jalil, M.K. Ahmed, Investigation of a novel window solar air collector with 7-moveable absorber plates, Energy 257 (2022).
[29] A. Chialastri, M. Isaacson, Performance and optimization of a BIPV/T solar air collector for building fenestration applications, Energy and Buildings 150 (2017) 200-210.

[30] C. Zhang, W. Gang, J. Wang, X. Xu, Q. Du, Experimental investigation and dynamic modeling of a triple-glazed exhaust air window with built-in venetian blinds in the cooling season, Applied Thermal Engineering 140 (2018) 73-85.
[31] T. Ulavi, T. Hebrink, J.H. Davidson, Analysis of a hybrid solar window for building integration, Solar Energy 105 (2014) 290-302.
[32] C. Shen, X. Li, Solar heat gain reduction of double glazing window with cooling pipes embedded in venetian blinds by utilizing natural cooling, Energy and Buildings 112 (2016) 173-183.
[33] C. Shen, X. Li, S. Yan, Numerical study on energy efficiency and economy of a pipe-embedded glass envelope directly utilizing ground-source water for heating in diverse climates, Energy Conversion and Management 150 (2017) 878-889.
[34] C. Shen, X. Li, Thermal performance of double skin façade with built-in pipes utilizing evaporative cooling water in cooling season, Solar Energy 137 (2016) 55-65.
[35] H. Choi, Y. An, K. Kang, S. Yoon, T. Kim, Cooling energy performance and thermal characteristics of a naturally ventilated slim double-skin window, Applied Thermal Engineering 160 (2019).
[36] C. Wang, N. Li, T. Gu, J. Ji, B. Yu, Design and performance investigation of a novel double-skin ventilated window integrated with air-purifying blind, Energy 254 (2022).
[37] P. Pfrommer, K.J. Lomas, C.J.S.E. Kupke, Solar radiation transport through slat-type blinds: A new model and its application for thermal simulation of buildings, 57(2) (1996) 77-91.
[38] Y. Wang, Y. Chen, Modeling and calculation of solar gains through multi-glazing facades with specular reflection of venetian blind, Solar Energy 130 (2016) 33-45.
[39] C. Guo, J. Ji, W. Sun, J. Ma, W. He, Y. Wang, Numerical simulation and experimental validation of tri-functional photovoltaic/thermal solar collector, Energy 87 (2015) 470-480.
[40] F. Khalvati, A. Omidvar, Summer study on thermal performance of an exhausting airflow window in evaporatively-cooled buildings, Applied Thermal Engineering 153 (2019) 147-158.
[41] A.J.N. Khalifa, R.H. Marshall, Validation of heat transfer coefficients on interior building surfaces using a real-sized indoor test cell, International Journal of Heat and Mass Transfer 33(10) (1990) 2219-2236.
[42] ISO 15099, Thermal performance of windows, doors and shading devices — Detailed calculations, (2003).
[43] T.E. Jiru, F. Haghighat, Modeling ventilated double skin façade—A zonal approach, Energy and Buildings 40(8) (2008) 1567-1576.
[44] J.H. Lienhard, A heat transfer textbook, Phlogistron2005.
[45] V. Gnielinski, New equations for heat and mass transfer in the turbulent flow in pipes and channels, NASA STI/recon technical report A 41(1) (1975) 8-16.
[46] R.K. Shah, A.L. London, Laminar flow forced convection in ducts: a source book for compact heat exchanger analytical data, Academic press2014.
[47] J. Ji, C. Guo, W. Sun, W. He, Y. Wang, G. Li, Experimental investigation of tri-functional photovoltaic/thermal solar collector, Energy Conversion and Management 88 (2014) 650-656.
[48] Z. Hu, W. He, D. Hu, S. Lv, L. Wang, J. Ji, H. Chen, J. Ma, Design, construction and performance testing of a PV blind-integrated Trombe wall module, Applied Energy 203 (2017) 643-656.
[49] A.G. ASHRAE, Guideline 14-2014: Measurement of energy, demand, and water savings, American Society of Heating, Refrigerating, and Air Conditioning Engineers, Atlanta, Georgia (2014).
[50] M. Wang, J. Peng, N. Li, H. Yang, C. Wang, X. Li, T. Lu, Comparison of energy performance between PV double skin facades and PV insulating glass units, Applied Energy 194 (2017) 148-160.

[51] WINDOW simulation software, Available online: https://windows.lbl.gov/software/window ([Accessed 2 June 2023]).
[52] Commercial Reference Buildings. Available online: https://www.energy.gov/eere/buildings/commercial-reference-buildings. [Accessed 5 June 2023].
[53] T. Formica, M. Pecht, Return on investment analysis and simulation of a 9.12 kilowatt (kW) solar photovoltaic system, Solar Energy 144 (2017) 629-634.
[54] Y. Luo, L. Zhang, Z. Liu, L. Xie, X. Wang, J. Wu, Experimental study and performance evaluation of a PV-blind embedded double skin façade in winter season, Energy 165 (2018) 326-342.
[55] C. Liu, Y. Lyu, C. Li, J. Li, K. Zhuo, H. Su, Thermal performance testing of triple-glazing water flow window in cooing operation, Solar Energy 218 (2021) 108-116.